Russian Chemical Reviews **81** (10) 936 – 959 (2012) © 2012 Russian Academy of Sciences and Turpion Ltd

DOI 10.1070/RC2012v081n10ABEH004281

Porous structure and wetting of fuel cell components as the factors determining their electrochemical characteristics

Yu M Volfkovich, V E Sosenkin

Contents

I.	Introduction	936
II.	Method of studying porous materials	937
III.	Components of fuel cell electrodes	939
IV.	Membranes	950
V.	The effect of the porous structure of membrane-electrode assembly components on the electrochemical characteristics of fuel cells. Optimization of the porous structure	954
VI.	Conclusion	957

Abstract. The results of studies of the principal components of the membrane-electrode assembly (ion-exchange and capillary membranes, polymer hydrophobization agents) obtained by standard contact porosimetry are considered. The phenomenon of inversion of ion-exchange groups of ionomers that affects the hydrophilic-hydrophobic properties of catalytic layers is described. The effect of the porous structure and wettability of components of the membrane-electrode assembly on the electrochemical characteristics of fuel cells is discussed. The bibliography includes 167 references.

I. Introduction

Fuel cells (FC) are converters of chemical energy to electricity in which (in contrast to storage batteries) the reactants are constantly supplied and the overall electrochemical reaction products are removed.[1,2] The majority of fuel cells consume hydrogen, methanol or ethanol as the fuel and pure oxygen or air oxygen as the oxidant. The heart element of FC is the membrane-electrode, which comprises an electrolyte-containing membrane and anodic and cathodic catalytic and gas-diffusion layers (Fig. 1). There are three types of electrolyte-containing membranes:

— capillary membranes with pores soaked with electrolyte solution, which are used in FC with alkaline and phosphoric acid electrolytes;

— proton-conducting membranes with polymer electrolytes soaked with water, which are used in FC with direct hydrogen or methanol (ethanol) oxidation;

— solid oxygen-conducting membranes based on zirconium oxide stabilized with yttrium oxide, which are used in high-temperature FC with solid oxide electrolytes.

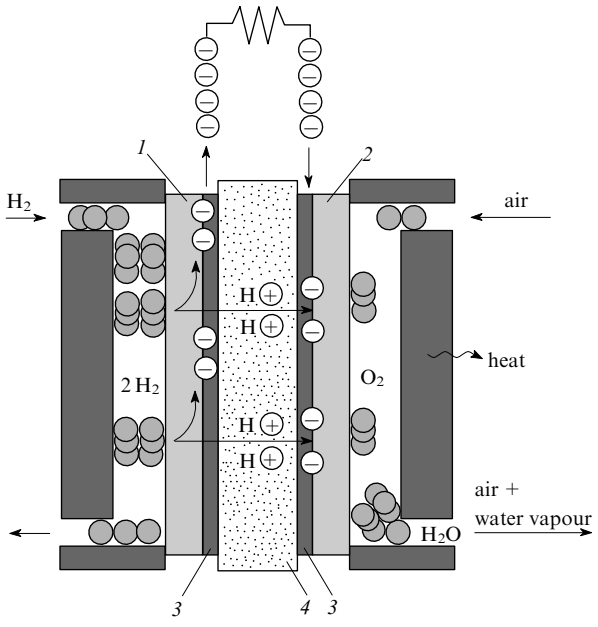


Figure 1. Illustration of a fuel cell.
(*1*) Gas-diffusion layer (anode), (*2*) gas-diffusion layer (cathode), (*3*) catalytic layers, (*4*) proton-exchange membrane.

Yu M Volfkovich, V E Sosenkin A N Frumkin Institute of Physical Chemistry and Electrochemistry, Russian Academy of Science, Leninsky prosp. 31, 119991 Moscow, Russian Federation.
Fax (7-495) 952 53 08,
tel. (7-495) 955 40 19, e-mail: yuvolf40@mail.ru (Yu M Volfkovich), vsosenkin@mail.ru (V E Sosenkin)

Received 1 November 2011
Uspekhi Khimii **81** (10) 936 – 959 (2012); translated by T Ya Safonova

The FC operation is sustained by flows of gaseous or liquid reactants and products of electrochemical reactions in the membrane-electrode assembly. The porous structure † and the hydrophilic-hydrophobic properties of various components of the membrane-electrode assembly substantially affect the magnitude and direction of these flows.[1–3] Their effect is commensurate with that of the catalyst activity and in certain cases, it is even more significant. For gaining better insight into the mechanisms of heat and mass transfer in FC, their mathematical simulation and optimization, it is necessary to know the porous structure and the properties of components of the membrane-electrode assembly. Low-temperature ($T < 120$ °C) FC using polymer ion-exchange membranes as the electrolytes contain water in both gaseous and liquid states. In electrodes of such FC, some of the pores mainly formed by metal catalyst particles exhibit hydrophilic properties, *i.e.*, they are readily wetted with water. The other pores mainly formed by carbonaceous particles are hydrophobic; they remain dry and serve as the transport channels for gas reagents (oxygen, hydrogen, *etc.*). The reliability and the service life of such FC depend on the features of so-called water management related to selecting the direction of flows of the water vapour and liquid water in the membrane-electrode assembly.[1,2]

The porous structure of a material is conventionally characterized by its porogram, *i.e.*, the pore volume (V) distribution *versus* pore radius (r) in either integral [$V(r)$] or differential [$(\mathrm{d}V/\mathrm{d}r)(r)$] form. The pore volume can be related to unit mass or unit volume of the material. The ratio of the total volume of pores to the material volume characterizes its porosity (υ).

By using the equation

$$S = 2\int_0^r \frac{1}{r}\frac{\mathrm{d}V}{\mathrm{d}r}\mathrm{d}r, \qquad (1)$$

it is possible to calculate yet another important parameter, the distribution of the pore surface (S) *versus* pore radius, *i.e.*, the $S(r)$ function. The pore surface area is often referred to unit weight of the material (specific surface area).

In the present review, we analyze in detail the information on the porous structure and hydrophilic-hydrophobic properties of FC components and also consider the effect of these properties on the electrochemical characteristics of FC. It should be noted that no reviews on this subject have appeared so far; only journal publications that reflect particular (but not all) problems associated with this very important branch of electrochemical power engineering are available.

II. Method of studying porous materials

1. Methods used to study the porous structure

A recent review [4] gives detailed account of various porosimetric techniques. The most widely used method of mercury porosimetry [5] is based on the dependence of the volume of mercury intruded into sample pores on the pressure. At the external pressure (P) being constant, all pores with $r > r_{\min}(P)$ are flooded with mercury. The quantity $r_{\min}$ corresponds to the following condition determined by the thermodynamic Laplace equation for capillary pressure (p_c):

$$p_c = -\frac{2\sigma\cos\theta}{r_{\min}}, \qquad (2)$$

where σ is the liquid surface tension at the lquid – vacuum or gas (air) interface for uncharged mercury $\sigma = 0.47$ N m^{-1}; θ is the contact angle at the three-phase mercury – sample pores – vacuum interface.

Using the dependence of the mercury volume intruded into the sample pores (V_{Hg}) on the external pressure, one can derive the distribution function of the pore volume *versus* pore radius over a very wide range of radii, namely, from ~ 2 to 10^5 nm. Mercury porosimetry is used extensively to study the porous structures of various materials; however, it is not free from serious drawbacks.

First, it requires very high pressures (up to several hundred megapascals), which results in deformation (or destruction) of many samples and, hence, distortion of porograms. Hence, this method cannot be used to study soft and brittle materials. Second, it cannot be applied to most metals, because they form amalgams with mercury (*e.g.*, Al, Cu, Zn, Cd, Ag, Sn, Pb, Au, Pt, Pd). Third, the exact value of the mercury contact angle is unknown for the majority of materials, which turns quantitative data processing into a fitting procedure. These drawbacks virtually rule out the application of mercury porosimetry to the principal components of FC, *i.e.*, membranes, gas-diffusion and catalytic layers that can be deformed under high pressures (moreover, the platinum catalyst layers can form amalgams). Fourth, mercury is toxic. At present, various modifications of mercury porosimetry that employ non-wetting liquids other than mercury (*e.g.*, water) are used to study hydrophobic materials.[6–10] Brittle and soft materials can also be destroyed upon the injection of water into the pores under high pressure; hence, this method is applied to sufficiently strong hydrophobic materials.

Other methods of studying the porous structure are known. Each method has some drawbacks and limitations. Small-angle X-ray scattering [11] can be used only if the pore radius is in the range from ~ 2 to 50 nm. Centrifugal porosimetry [12] and optical techniques are virtually useless if the pore size is < 1 μm. The porous diaphragm method [13] (more recently referred to as liquid porosimetry [14]) based on forcing out of a wetting liquid from the pores under gas pressure is used only for coarse pores (r from 1 to 1000 μm). The capillary condensation method [15] can be used for pore size in the range from ~ 1 to 50 nm. The method of low-temperature nitrogen adsorption is employed for estimating the specific surface area of porous materials.[15] The use of microscopic techniques [16–20] is faced with complications of sample preparation and quantitative interpretation of results. Microscopic methods always employ computer programmes for calculating the pore and particle size distributions [21] and specific surface areas based on scanned images,[22] which makes it possible to acquire quantitative results. However, it is desirable to compare the results of such calculations with the corresponding characteristics found by conventional methods, for instance, mercury porosimetry, capillary condensation or low-temperature nitrogen adsorption.

† Hereafter the term porous structure means the geometry and shape of pores and pore size distribution.

2. Methods of studying hydrophilic-hydrophobic properties

Hydrophilic-hydrophobic properties of porous materials are determined by the contact angle between the pore surface and a liquid and also by the volumes of hydrophilic and hydrophobic pores. Such properties of materials with smooth surfaces can be characterized by the contact angle formed by a water drop placed on this surface. However, this method cannot be used for porous materials because the surface roughness distorts the contact angle. Moreover, this method characterizes the properties only of the external surface rather than that of internal pores.

In 1921, Washburn [23] developed a method for determination of the internal contact angle for a porous sample, which is based on the rate of water rise in a hanging sample. However, his method is inapplicable to virtually hydrophobic samples. Later,[24,25] this experimental technique was refined and a better procedure was proposed for mathematical processing of the results,[24,26–31] which took into account not only the surface tension and viscosity of the liquid but also gravity and inertia. Nevertheless, the Washburn method gives no way for determining the dependence of the contact wetting angle on the pore radius, which is important for FC.

3. Standard contact porosimetry

The drawbacks and limitations of methods used to study the porous structure of materials and their hydrophobic-hydrophilic properties have stimulated the development of a new method, namely, standard contact porosimetry.[32–34] This method was described in detail in several publications.[35–38]

a. The fundamentals of the method

The method of standard contact porosimetry relies on the following fact. When a liquid is distributed between pores in porous solids (1, 2, ..., i) brought in contact with each other and occurring in the state of capillary equilibrium, the interfacial (between dry and flooded pores) capillary potentials (Ψ_i) are equal

$$\Psi_1 = \Psi_2 = \ldots \Psi_i = \Psi. \tag{3}$$

The following quantities can be used as analogues of the capillary potential: p/p_s (p, p_s are the liquid vapour pressure in the pores and the saturated vapour pressure, respectively), the capillary pressure p_c, the free binding energy between the liquid and the porous solid (A).

The curve of the relative moisture content, *i.e.*, the equilibrium dependence of the moisture content in the sample under study (v_1) on the moisture content of a standard porous sample (v_2), is measured

$$v_1 = \Phi(v_2). \tag{4}$$

The amount of liquid in the set of porous solids changes due to evaporation, impregnation, condensation or capillary suction. Preliminary calibration is done to determine the liquid volume distribution function over Ψ for the reference sample, *i.e.*, its potential-determining function

$$v_2 = f_2(\Psi). \tag{5}$$

Based on equations (3)–(5), the analogous potential-determining function is obtained for the sample under study

$$v_1 = \Psi(f_2(\Psi)) \equiv f(\Psi). \tag{6}$$

b. Possibilities of standard contact porosimetry for studying porous materials

Standard contact porosimetry has the following advantages over other methods, particularly, over mercury porosimetry:

— it can be used to measure pores with the radius from ~ 1 to 3×10^5 nm (the lower limit is the same as for the capillary condensation method);

— gives error of $\sim 1\%$ of the total pore volume;[38]

— can be applied to any material, for instance, frail, soft, brittle and even powdered samples;

— can be used to study samples at specified values of compression pressure and temperature, which allows the real operational conditions to be reproduced for various articles and devices;

— working liquids used in electrochemical devices (*e.g.*, water) can be used for measurements; hence, it is possible to study the real porous structure of a sample taking into account its swelling in the working liquid;

— repeated measurements on the same sample are possible, because the sample structure remains unchanged; the repeated measurements make it possible to reveal structural changes in the course of engineering processes;

— quantitative information on the corrugation of pores with variable cross-section can be acquired.[38]

Thus, the standard contact porosimetry provides a variety of data. Moreover, it is easily implemented and safe (non-toxic), in contrast to mercury porosimetry.

c. Studying the porous structure

The quantities p/p_s, p_c and A are interrelated by thermodynamic relationships

$$p_c = -\frac{2\sigma\cos\theta}{r} = \left(\frac{RT}{V_m}\right)\ln\frac{p}{p_s} = -\frac{A}{V_m}, \tag{7}$$

where V_m is the molar volume of the liquid.

Based on Eqns (6) and (7), it is possible to obtain the function of moisture content distribution over p/p_s, p_c and A. The function $v(p/p_s)$ is the isotherm of desorption (or adsorption), $v(p_c)$ is the isotherm of capillary pressure and the function $v(A)$ is the energy isotherm. The transition from v_i to the pore volume V is the same as in the method of capillary condensation. In the region of mesopores with r of about 1.5 to 50 nm, the presence of an adsorption film on the mesopore surface is taken into account.[15] Insofar as according to Eqn (7), the quantities p/p_s, p_c and A are related to the pore radius r, it is possible to pass from the adsorption isotherm $v(p/p_s)$ to the pore volume distribution *versus* radius (porosimetric curve or porogram). The porous structures are studied most often using octane and decane, which wet any material almost perfectly ($\theta \approx 0^\circ$), as the measuring liquids, while water is used to study the hydrophilic-hydrophobic properties. The amount of liquid in each porous sample is determined by weighing on electronic balance.

The standard contact porosimetry allows for the control over the capillary equilibrium in each point of the experimental curve.[38] For this purpose, two references are used in the measurements with the studied sample in between. The samples and the references are pressed together by a special clamping device with controllable compression pressure. The FC membrane-electrode assembly (see Fig. 1) involving

a membrane and catalytic and gas-diffusion layers brought into contact with one another serves as the prototype for the standard porosimeter. The electrolyte (water) is present in pores of all porous components. The electrolyte (water) distribution among these components is described by the laws of capillary equilibrium and expressions (3)–(7). The specially developed stable ceramic standards are calibrated using mercury porosimetry and capillary condensation techniques and electron microscopy. For details of measurements, see Refs 35–38. The chief disadvantage of the standard contact porosimetry is the long time required for the measurements due to the large number of manual procedures associated with assembling and disassembling of the set of porous samples and placing them on the balance. However, in recent years, a robotized automatic standard porosimeter was developed,[39,40] which substantially accelerated and facilitated the procedure.

d. Study of hydrophilic-hydrophobic and sorption properties of porous materials

Among the most important advantages of standard contact porosimetry as compared with mercury porosimetry and other methods is the possibility of measuring hydrophilic-hydrophobic or lyophilic-lyophobic properties of porous materials. It was shown[37,38] that it is possible to determine the contact wetting angle directly in the pores by using various measuring liquids. For this purpose, the pore volume distribution *versus* parameter $r^* = r/\cos\theta$, *i.e.*, the effective pore radius, is measured by standard contact porosimetry with the use of octane and the liquid under study (most often, water). For materials poorly wetted by water with $\theta > 0^\circ$, the porosimetric curve measured using water is shifted to higher r^* values as compared with the corresponding curve measured with octane. Based on this shift, for a given pore volume V_i and the corresponding pore radius r_i, the contact angle is determined as

$$\cos\theta_i = \frac{r_i}{r_i^*}. \qquad (8)$$

Thus the $\theta(r)$ dependence is obtained, which is impossible by any other method.

For studying porous materials which either swell or are poorly wetted in certain electrolyte solutions and water, particularly these solutions or solvents, *e.g.*, water, should be taken as the measuring liquids. Thus, the porous structure of the material under study is modelled under the conditions resembling most closely the real operation conditions.

These advantages and possibilities of the method of standard contact porosimetry find wide application in studying various FC components and processes occurring therein.

III. Components of fuel cell electrodes

1. Catalytic layer

Anodic and cathodic catalytic layers are the principal components of FC, because it is in these layers that electrode reactions generating electricity occur. The catalytic layer of FC with proton-conducting membrane (proton-exchange membrane FC) represents a complex composite system which, in the general case, contains platinum metal particles deposited on a particulate carbon support; hydrophobic particles, mainly, polytetrafluoroethylene (PTFE); and ionomer particles, mainly, Nafion (Fig. 2). The ionomer swelled in water provides proton conduction. Liquid water transport in the catalytic layer occurs through hydrophilic pores in the carbon support and in the ionomer, while active gases (oxygen and hydrogen) are delivered to the catalyst surface and the reaction products (water vapour) are removed through the hydrophobic pores. The carbon support-to-ionomer volume ratio determines the electronic and ionic conductivities. The structural and hydrophilic-hydrophobic properties of the catalytic layer components largely affect the FC efficiency.

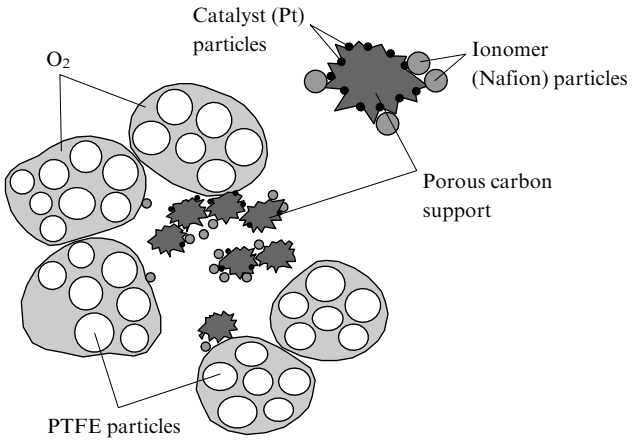


Figure 2. Illustration of the catalytic layer structure of the cathode of a proton-exchange membrane FC.

a. Porous structure of the catalytic layer

The standard contact porosimetry was used[41] to study a catalytic layer manufactured by E-TEK Company that contained 40 mass % of Pt deposited on Vulcan XC-72 carbon black and 5 mass % of Nafion deposited from an ethanol solution. These studies were insufficiently systematic and did not include experiments with other types of carbon supports. Several works were devoted to detailed studies of the porous structure of various carbon supports and also to the changes in this structure after different stages of catalytic layer preparation.[42–44] Table 1 shows the main characteristics of the porous structure of the studied carbon supports measured before and after the introduction of 17 mass % of the Nafion ionomer. The range of S values for these supports was very wide, from 15 to 980 $m^2\ g^{-1}$.

Upon the introduction of the iomomer, the total specific volume of pores increases as a result of formation of new intergrain pores. At the same time, the intergain specific pore volume decreases. This can be explained by the pore mouth blockage by ionomer particles; for some carbon supports, this decreases the fraction of pores with $r < 1$ nm, although the ionomer particle size is much larger (> 10 nm). The blockage also reduces the inner surface area of mesopores. For different supports, different degrees of blockage were found. Figure 3 shows the integral porograms for the activated carbon Anderson Ax-24 measured before and after the introduction of 17 mass % of Nafion ionomer. It is seen that after the ionomer introduction, the specific volume of pores with $r < 1$ μm considerably

Table 1. Principal characteristics of the porous structure of carbon supports before (numbers above the line) and after (numbers below the line) the introduction of 17 mass % of Nafion ionomer.[42]

Carbon support	V/cm^3 g^{-1}	V_1/cm^3 g^{-1}	V_2/cm^3 g^{-1}	V_{mic}/cm^3 g^{-1}	S/m^2 g^{-1}	S_{mes}/ m^2 g^{-1}
Anderson Ax-24	1.08	0.81	0.27	0.36	980	8
	1.78	0.48	1.3	0.23	627	7
Sibunit 619P	1.51	0.85	0.66	0.06	380	205
	1.74	0.704	1.036	0.13	488	130
Vulcan XC-72	2.22	1.69	0.53	0.06	255	140
	2.87	1.32	1.55	0.044	105	97
Sibunit 20P	0.86	0.53	0.33	0.05	230	132
	1.52	0.5	1.02	0.12	330	100
KBU-2 (see [a])	1.10	0.51	0.59	0.06	208	92
	1.67	0.37	1.3	0.03	121	53
P-267E	2.73	2.1	0.63	0.02	180	150
	2.82	1.52	1.3	0.01	150	130
P-324	1.23	1.1	0.13	0	125	125
	1.69	0.95	0.74	0	54	53
KBU-1 (see [b])	0.69	0.29	0.4	0.02	95	47
	1.33	0.22	1.11	0.01	60	38
Sibunit 19P	0.51	0.33	0.18	0.02	70	38
	0.83	0.214	0.616	0.03	80	21.5
P-702	0.97	0.81	0.16	0	32	32
	1.64	0.67	0.97	0	14	14

Note. Porous layers of all carbon supports include the grain (primary) structure with pore radii of $< 10^3$ nm, mainly in the range from 0.3 to 50 nm (specific volume of these pores V_1) and the intergrain (secondary) structure with pore radii of $> 10^3$ nm (specific volume of these pores is V_2); V_{mic} is the specific volume of micropores, S is the total specific surface area of pores, S_{mes} is the specific surface area of mesopores. [a] Nanofibres with graphene sheets packed in the fence pattern. [b] Nanofibres packed in the herring-bone pattern.

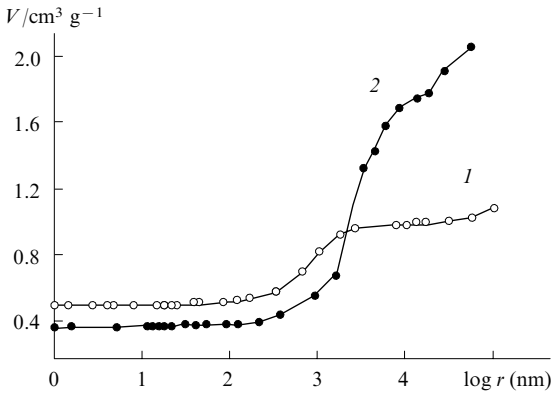


Figure 3. Integral porograms for active carbon Anderson Ax-24 before (*1*) and after (*2*) the introduction of 17 mass % of Nafion ionomer.[42]

decreases. The ionomer effect was also similar for other carbonaceous materials, *e.g.*, for Vulcan XC-72 carbon black, which is often used as the support for FC catalysts. For nanofibres KVU-1, almost no decrease in the specific volume of pores with $r < 10^3$ nm was noted. It was shown [42–44] that the degree and the character of pore blockage in a carbon support by ionomers depend on the pore geometry. Presumably, the character of blockage depends on the nature of ionomer functional groups and the carbon surface coverage by these groups.

b. Hydrophilic-hydrophobic and sorption properties of the catalytic layer

The hydrophilic-hydrophobic and sorption properties of carbon supports listed above were studied (see Table 1) before and after the introduction of Nafion.[43,44] The majority of supports (Vulcan XC-72, P-324, P-702, Anderson Ax-24, P-267E and Sibunit 619P) become more hydrophobic upon ionomer introduction, whereas some other supports (*e.g.*, KVU-1 fibres) become more hydrophilic (Figs 4 and 5). There exists the third (intermediate) group of carbon materials (KVU-2, Sibunit 19P and Sibunit 20P) the pore surface of which becomes more hydrophobic for pores of certain size and more hydrophilic for pores of other sizes. Thus, upon the introduction of an ionomer, Vulcan

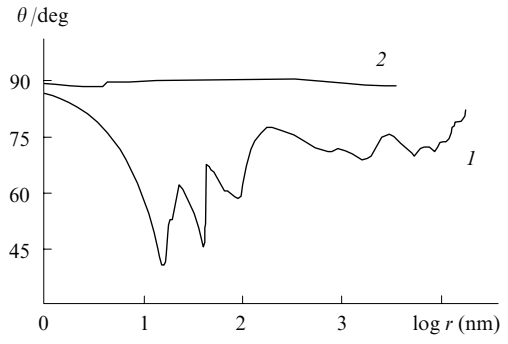


Figure 4. Dependences of the contact angle with water on the pore size for Vulcan XC-72 carbon black before (*1*) and after (*2*) the introduction of 17 mass % of Nafion ionomer.[43]

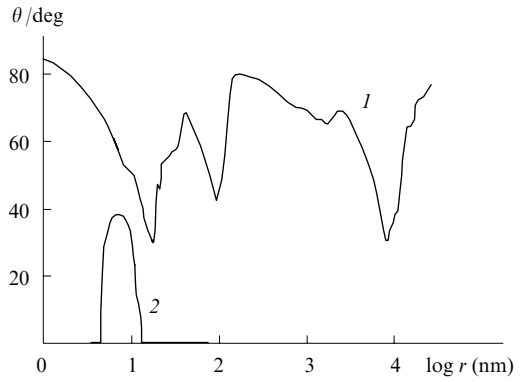


Figure 5. Dependences of the contact angle with water on the pore size for KBU-1 nanofibres before (*1*) and after (*2*) the introduction of 17 mass % of Nafion ionomer.[43]

XC-72 is hydrophobized (its contact angle increases throughout the whole range of pore radii) whereas KVU-1 nanofibres are hydrophilized. These results can be explained by the inversion of sulfo groups (and/or some other ionic groups of ion-exchange resins and membranes) with respect to the polymer chain (Figs 6, 7).

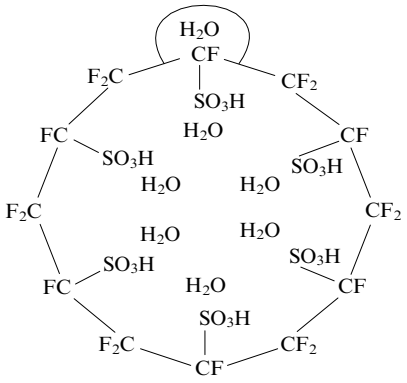


Figure 6. Illustration of an ionomer particle deposited on Vulcan XC 72 carbon black with sulfo groups oriented inwards the PTFE chain.[43]

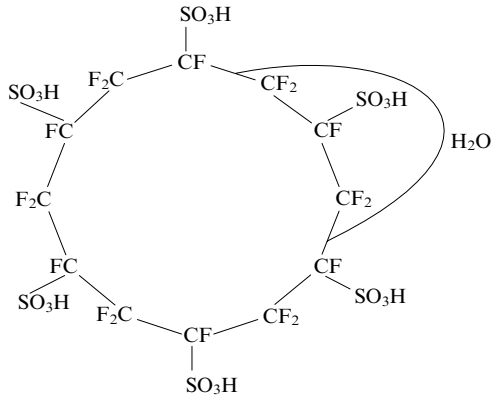


Figure 7. Illustration of an ionomer particle deposited of KBU-1 nanofibres with sulfo groups oriented outwards the PTFE chain.[43]

The orientation of sulfo groups on the surface of ionomer particles depends to a considerable extent on their ability to be adsorbed on the surface of carbon supports. The surface properties of a material are determined by the nature and concentration of functional groups formed during its preparation and located on its surface. When sulfo groups point inside the chain (see Fig. 6), the hydrophobic perfluorinated chains $(-CF_2-CF_2-)_n$ occur on the surface, which results in hydrophobization of the catalytic layer; for the opposite orientation (see Fig. 7), sulfo groups are outside, which leads to hydrophilization of the catalytic layer. The ionomer-induced hydrophobization is unusual, because the internal space of the ionomer is obviously hydrophilic due to hydration of sulfo groups.

Hence, an ionomer can serve as both the second-class proton conductor and the hydrophobizing or hydrophilizing agent for the catalytic layer. This is practically important for optimization of the catalyst structure in a fuel cell. For instance, several firms working on the proton-exchange membrane FC comprizing Vulcan XC-72 carbon black recently ceased to add a special hydrophobizer, dispersed PTFE, to catalytic layers containing Nafion without giving any reason.[45] Probably, they have empirically ascertained that the delivery of oxygen and hydrogen to the catalyst surface is not the rate-limiting stage of electrochemical reactions, which can be attributed to the ionomer-induced hydrophobization of Vulcan XC-72 observed experimentally.[43,44] Moreover, the revealed effect is consistent with the hydrophobic properties of the surface of Nafion type membranes.[46]

Thus, the authors cited [43,44] observed for the first time the phenomenon of orientational inversion of sulfo groups in the external layer of Nafion particles depending on its contact with various carbonaceous materials.

The orientational inversion of ion-exchange groups with respect to the polymer chain was also observed [47] for ion-exchange groups in composite sulfonated phenol cation exchange membranes of the Polycon type. Perhaps, this phenomenon is typical of many ion exchangers and, in the general case, it can be represented as the template effect of the support surface on the structure of very thin deposited layers [48,49] (the inversion of ion-exchange groups occurs only in the $\sim$1 nm-thick surface layer of the ionomer).

Table 2 shows the characteristics of the porous structure of certain carbon supports before and after deposition of platinum and Nafion ionomer. It is evident that deposition of platinum on Sibunit materials induces an increase in their hydrophilic surface area and a decrease in θ, *i.e.*, their hydrophilization, which is due to hydrophilicity of platinum. At the same time, the introduction of 17 mass % of Nafion into the systems Sibunit 19P + 10 mass % Pt and Sibunit 20P + 30 mass % Pt induced their partial hydrophobization.

Figure 8 shows the energy isotherms $v(A)$ for Sibunit 20P carbon black samples. The quantity A in the range of six orders of magnitude was calculated according to Eqn (7) based on porosimetric curves measured in different stages of catalytic layer preparation. The isotherms characterize the interaction of water with this material. As A increases, the nature of this interaction changes as follows: simple flooding of progressively finer macropores, capillary condensation of vapour first in mesopores and later in micropores, hydration of ion-exchange groups and, finally, adsorption. Thus, the energy isotherms describe in more detail the water

Table 2. Characteristics of the structure of Sibunit 19P and Sibunit 20P carbon blacks before and after the deposition of platinum and Nafion ionomer.

Study object	v /cm^3 cm^{-3}	S /m^2 g^{-1}	v_{phil} /cm^3 cm^{-3}	S_{phil} /m^2 g^{-1}	θ /deg
Sibunit 19P	0.5	70	0.39	20	74
Sibunit 19P + Pt (10 mass %)	0.64	105	0.64	40	49
Sibunit 19P + Nafion (17 mass %)	0.62	80	0.62	27	79
Sibunit 19P + Pt (10 mass %) + Nafion (17 mass %)	0.59	91	0.55	69	59
Sibunit 20P	0.63	230	0.47	53	75
Sibunit 20P + Pt (30 mass %)	0.77	324	0.74	67	51
Sibunit 20P + Nafion (17 mass %)	0.75	332	0.65	30	70
Sibunit 20P + Pt (30 mass %) + Nafion (17 mass %)	0.71	282	0.63	171	64

Note. The following designations are used: v and v_{phil} are the total and hydrophilic porosity, respectively; S and S_{phil} are the total and hydrophilic surface areas, respectively; θ is the average contact angle with water.

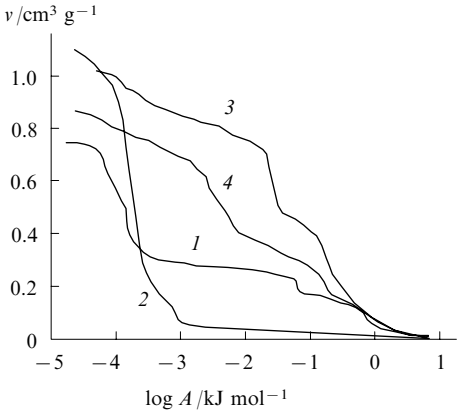


Figure 8. Energy isotherms for Sibunit 20P carbon black before (*1*) and after the introduction of 17 mass % of Nafion ionomer (*2*), 30 mass % of Pt (*3*), 30 mass % of Pt + 17 mass % of Nafion ionomer (*4*).[43]

interaction with the components of the catalytic layer as compared with conventional $v(p/p_s)$ isotherms.

In conclusion, note that no method other than the standard contact porosimetry makes it possible to acquire detailed and diversified information on the porous structure and hydrophilic-hydrophobic properties of so complicated composite object as the catalytic layer.

2. Catalysts used in fuel cells

a. Platinum catalysts

Despite the high cost of catalysts containing platinum-group metals, they are used most often in low-temperature FC because other metals exhibit much lower specific catalytic activities. The structure of platinized platinum (Pt/Pt) and platinum black (Adams platinum) was studied.[50] Platinum black samples were pressed into pellets under a pressure of 150 MPa. Both materials possessed considerable volumes of micropores with $r < 1$ nm; moreover, in Pt/Pt, this volume was approximately half of the total pore volume. The radii of the majority of other pores did not exceed 3 nm. This result is important because the size of micropores is comparable with the thickness of the electric double layer in not too dilute solutions[51] and exceeds the size of many ions and molecules, especially, organic, by no more than one order of magnitude. These factors affect the adsorption properties and the catalytic activity of these catalysts.[52]

b. Platinum – fluoropolymer composites

To accelerate the delivery of gaseous regents (O_2, H_2) to the catalyst, the latter was hydrophobized usually by introducing PTFE particles. The Pt – PTFE composite is a multicomponent porous system with mixed hydrophilic-hydrophobic properties. At present, the unsupported Pt – PTFE system is used very rarely, mainly in FC with alkaline or phosphoric acid electrolytes.[53,54] However, this system can serve as a model in studying the hydrophilic-hydrophobic properties and the porous structure of more complicated electrocatalytic systems. It was shown[37] that for a two-component system with contact angle with water (or aqueous solutions) of y_1 for the hydrophilic component (metal catalyst) and y_2 for the hydrophobic component (PTFE), the mean contact angle can be calculated according to the equation

$$\cos\theta \equiv (1-\rho)\cos\theta_1 + \rho\cos\theta_2 > 0\,, \qquad (9)$$

where ρ is the hydrophobicity factor (the surface fraction of pores occupied by the hydrophobic component).

Platinum – PTFE electrodes prepared from a suspension of PTFE (brand F-4D) were studied by standard contact porosimetry.[55] Porosimetric experiments were carried out with the use of several liquids with different wetting capacity with respect to PTFE (θ_{PTFE}): heptane (24°), toluene (49°), acetophenone (73°), furfural (80°), 5% methyl ethyl ketone in water (90°), 1% methyl ethyl ketone in water (100°), water (108°), *etc*. Based on porograms obtained, the differential distribution functions ($\partial^2 V/\partial r\,\partial\log r$) of pore volume *versus* pore radius and *versus* hyrophobicity factor were calculated. Figure 9 shows such function of two variables for a platinum – fluoropolymer electrode with 16 mass % of PTFE. The function has three maxima: two for hydrophilic pores and one for hydrophobic pores. From this dependence, which cannot be obtained by any other method, it follows that the structure of the Pt – PTFE electrode has only two types of pores: completely hydrophilic pores ($\theta_{Pt} < 90°$) located inside platinum agglomerates between the particles and completely hydrophobic pores ($\theta_{PTFE} > 90°$) located inside PTFE agglomerates.

A macrokinetic theory was developed,[55,56] which is suitable for calculating polarization curves (current density *vs*. polarization) for hydrophobized electrodes. In the

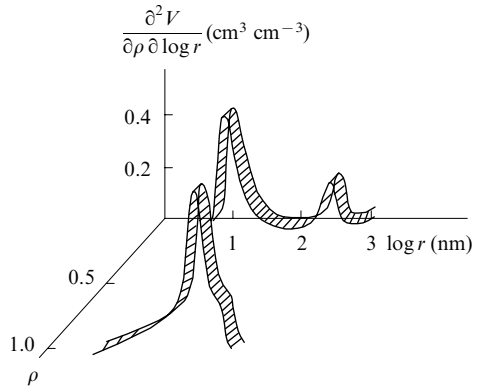


Figure 9. Function $\partial V/\partial\rho\,\partial\log r$ *vs.* $\log r$ for the electrode Pt + 16 mass % PTFE.[55]

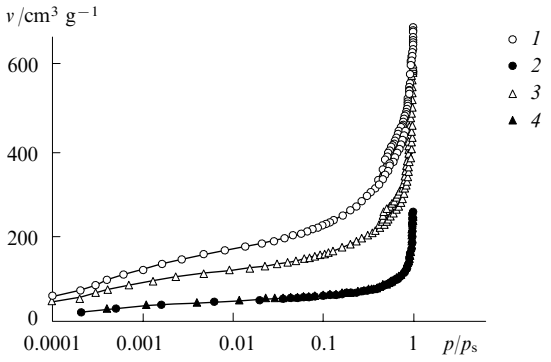


Figure 10. Nitrogen adsorption isotherms on Ketjenblack (*1*) and Vulcan XC-72 (*2*) carbon blacks and also on Pt/Ketjenblack (*3*) and Pt/Vulcan XC-72 (*4*) catalytic layers.[57]

derived equations, one of the main parameters is the specific interfacial area (S_s) between two porous agglomerates consisting of platinum and PTFE particles. This interface can comprise four phases because the pores situated inside platinum agglomerates contain liquid electrolyte, while the pores in PTFE agglomerates contain active gas.

A method was proposed[53] for the determination of S_s for Pt – PTFE electrodes, which involves the following main stages: decane-based measurements of a porogram of all pores of the original electrode [$V_\Sigma(\log r)$]; water-based measurements of a porogram of hydrophilic pores in the original electrode [$V_{phil}(\log r)$]; the removal of PTFE from the electrode by its decomposition at 400 °C; decane-based measurements of a porogram $V_r(\log r)$ for the resulting electrode (under the assumption that the size of platinum agglomerates remains virtually unchanged); plotting the radius distribution of PTFE agglomerates [$V_{ag}(\log r_{ag})$]. The quantity S_s was determined by integration of the $V_{ag}(\log r_{ag})$ curve according to expression (1). For the platinum – PTFE electrode under study, which contained 4 mass % PTFE, it was found that $S_s = 3 \times 10^4$ cm^2 cm^{-3}. The resulting $V_{ag}(\log r_{ag})$ curve has demonstrated that the range of diameters of agglomerated PTFE particles in the electrode varies from ~0.1 μm to several tens of micrometers with the maximum at 0.1 – 0.3 μm. Based on the S_s values thus found,[53] the polarization curves were calculated for the cathodic reaction of oxygen electroreduction in 30% aqueous KOH. A comparison of experimental polarization curves and those built based on the simplified Butler – Volmer equation[51] demonstrated their adequate agreement.[53]

c. Carbon-supported platinum catalysts

Finely dispersed carbon materials with high electric conductivities and large specific surface areas serve traditionally as supports for platinum catalysts. Carbon blacks are the most popular carbon supports of which Vulcan XC-72 manufactured by E-TEK company is used most widely. There are publications in which carbon black surface layers were studied before and after the deposition of platinum catalysts by means of the methods of Brunauer – Emmett – Teller (BET), scanning electron microscopy (SEM) and transmission electron microscopy (TEM).[57–64] Deposition of platinum catalyst particles on Ketjenblack carbon black was shown[57] to substantially reduce the volume of micro- and mesopores and the support specific surface area, whereas for Vulcan XC-72 carbon black, these values remained virtually unchanged. Figure 10 shows the corresponding isotherms of nitrogen adsorption. For a Pt/Ketjenblack catalytic layer, the volumes of micro- and mesopores were observed to decrease after the deposition of platinum. Using standard contact porosimetry, it was found[42] that the electrochemical deposition of platinum on Sibunit 19P and Sibunit 20P carbon blacks (in amounts of 10 mass % and 30 mass %, respectively) results in a relatively small increase in the volumes of micro- and mesopores and also in the specific surface areas of samples. This can be seen in porograms presented in Fig. 11.

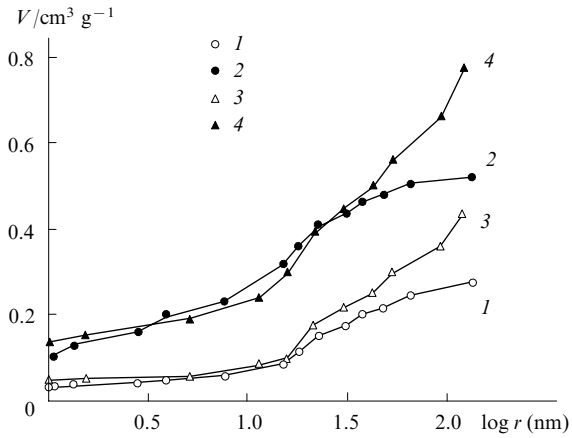


Figure 11. Integral porograms of Sibunit 19P (*1*) and Sibunit 20P (*2*) carbon blacks and also of Pt/Sibunit 19P (*3*) and Pt/Sibunit 20P (*4*) catalytic layers.[42]

Thus, for some types of carbon black, platinum deposition leads to plugging of fine pores, whereas, for other types, the pores remain open. It can be assumed that these differences (like the differences in the adsorption properties as regards ionomers) are caused by the peculiarities of adsorption of platinum particle precursors on the surface of different carbon supports and, probably, can be explained by the specific features of functional groups of the latter. Relatively small volume quantities of platinum have weak effect on porosimetric curves in the Pt – carbon

support system; it should be borne in mind that the density of platinum is an order of magnitude higher than the support density. The effect is least for carbon supports with great surface areas. However, the deposition of platinum gives rise to much more pronounced modifications in the surface properties of materials (towards hydrophilization).[43] This is evident, for instance, for the dependences of the contact angle on the pore radius in Sibunit 19P carbon black before and after the deposition of 10 mass % of Pt (Fig. 12). Based on the porosimetry data, it is possible to indirectly elucidate the positions of platinum particles (inside or outside fine pores), which can substantially affect the electrochemical characteristics of catalysts under the condition of gas-diffusion limitations on the access of reagents into these particles.

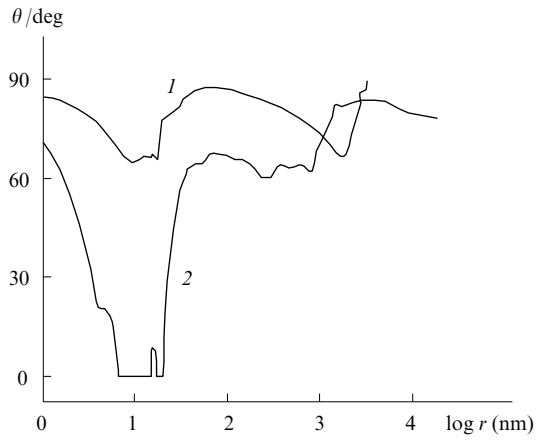


Figure 12. Contact wetting angle *vs*. the pore radius for Sibunit 19P active carbon (*1*) and Pt/Sibunit 19P catalytic layer (*2*).[43]

It was studied[60] how the specific surface areas of the carbon blacks (S_{carbon}) serving as supports for Pt–Ru catalysts affect the catalyst specific surface area (S_{Pt-Ru}) determined with respect to CO adsorption, the average size of metal particles (d_{Pt-Ru}) and the catalytic activity towards methanol electrooxidation. It was found that as S_{carbon} increased, the parameter S_{Pt-Ru} first sharply increased and then gradually flattened at $S_{carbon} \approx 500$ m^2 g^{-1}. Conversely, the values of d_{Pt-Ru} decreased with increase in S_{carbon}. The increase in Pt–Ru from 10 mass % to 50 mass % induced an increase in d_{Pt-Ru} due to agglomeration of metal particles. The specific activity (calculated in relation to true surface area) of the Pt–Ru catalyst increased with the increase in its amount to reach a maximum at $d_{Pt-Ru} = 4$ nm. For d_{Pt-Ru} below and above 4 nm, the specific activity was lower.

Many recent publications noted the enhanced catalytic activity in FC reactions for catalysts supported on carbon nanotubes.[65–74] For instance, the specific currents of methanol oxidation in relation to platinum weight were compared for platinum deposited on single-walled carbon nanotubes (SWNT) and on Vulcan XC-72.[65] The currents turned out to be three times higher in the former case. The catalytic effect with respect to methanol oxidation for catalysts deposited on various carbon nanotubes was also reported in some other publications.[66,69–72] The enhanced catalytic activity was attributed to the high specific surface area and electric conductivity of carbon nanotubes and also to the presence of oxygen-containing functional groups on their surface.

A higher catalytic activity of nanotube-supported platinum was also observed in the reaction of oxygen reduction.[73,74] These results supplement the information on the dependence of catalyst properties on the nature and structure of carbon supports. However, as a rule, in the majority of studies, the combined effect of different factors was considered. It is often assumed that a higher support dispersivity (for instance, on going from carbon black to nanotubes) means the higher catalyst specific surface area and, hence, the higher current density per unit catalyst weight. At the same time, the support can affect the rate constant of the reaction that proceeds on platinum and, to explore this possibility, the detailed information on the catalyst true surface area is necessary.

Insofar as fuel cells with polymer electrolytes operate in aqueous media, it is important to study the hydrophilic-hydrophobic properties of SWNT. The studies of their porous structure and hydrophilic-hydrophobic properties and also of their effect on the structure of deposited Pt–Ru and Pt catalysts and the electrochemical activity in methanol electrooxidation and oxygen electroreduction were carried out by the method of standard contact porosimetry.[73,74] For the synthesis of SWNT, the electric arc method with a nickel – yttrium catalyst was chosen; the resulting tubes were cleaned from amorphous carbon and the catalyst metals. According to the data of Raman spectroscopy, the nanotubes had a narrow pore diameter distribution (the mean diameter was $\sim$1.5 nm). Figure 13 shows a TEM image of a SWNT. The pores of nanotubes lack tortuosity; this favours the high specific conductivity of electrolyte in such pores.

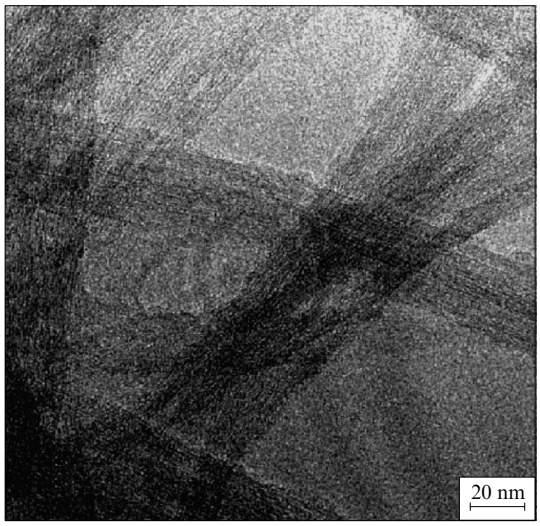


Figure 13. SEM Image of a single-walled carbon nanotube.[73]

To make their surface hydrophilic, a part of SWNTs was subjected to functionalization by treating them with a mixture of nitric and sulfuric acids to create hydroxyl and carbonyl groups at nanotube ends. Figure 14 shows the integral curves of the pore volume distribution *versus* effective radius (r^*) for original and functionalized SWNT

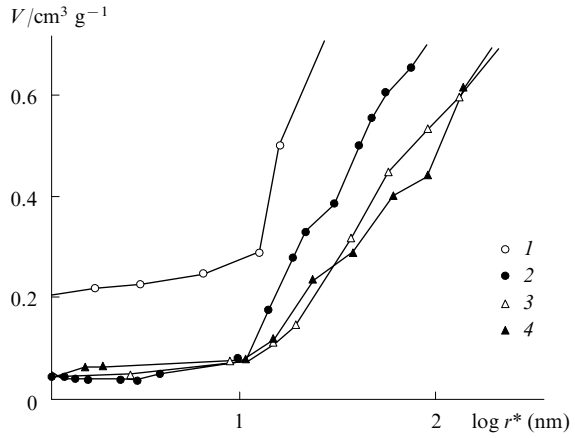


Figure 14. Integral porograms measured with the use of octane (*1*, *3*) and water (*2*, *4*) for the original (*1*, *2*) and functionalized (*3*, *4*) single-walled carbon nanotubes.[73]

($SWNT_f$). It is seen that the original SWNT are to a large extent hydrophobic; moreover, their micropores are completely hydrophobic. Taking this into account, we assume that no electrochemical reactions proceed inside SWNT in proton-exchange membrane FC. This conclusion is true for other types of FC with polymer electrolytes, because organic molecules are large as compared with the inner diameter of SWNT pores. Hence, it can be assumed that electrochemical reactions mainly occur on the external surfaces of SWNT, *i.e.*, in the pores formed inside their bundles (bunches of tubes).

In certain publications, the contact angles of nanotubes and microcapillaries of rather large diameters (from 40 to 800 nm) were studied for different liquids. Nanotubes and microcapillaries were made of various materials (carbon, glass, alumina, *etc.*).[75–81] The experiments were carried out by the classical and modified versions of the Washburn method[23] and also by photographing liquid drops on the external walls of nanotubes and capillaries. Note that these methods cannot be applied to SWNT with the inner diameter of about 1–2 nm. The static and dynamic filling of the inner space of carbon nanotubes by liquids and their wettability were modelled.[79,80,82–88] The model took into account molecular interactions in the liquid–carbon system, the distributions of viscosity and surface tension at nanometre distances, van der Waals forces, the roughness of the nanotube inner surface, the nature of surface, the concepts of molecular dynamics and also the conclusions[89] drawn based on the data on the meniscus curvature in the capillaries. The distribution of water over the inner radius of carbon nanotubes was calculated.[87] From our viewpoint, the results of these simulations cannot yet be used to predict the real processes in FC. The menisci formed by liquids in nanotubes with diameters of about ~1 nm can hardly be considered as the reasonable approximation.

Functionalized SWNT are virtually hydrophilic (see Fig. 14). Table 3 shows the total and hydrophilic specific surface areas determined for Vulcan XC-72 and original and functionalized SWNT by contact porosimetry and also the specific surface areas of Pt–Ru catalysts. The true

Table 3. Total and hydrophilic specific surface areas of SWNT, $SWNT_f$ and Vulcan carbon black and also specific surface area of Pt–Ru catalyst electroplated on these supports.

Total specific surface areas measured with octane /m^2 g^{-1}			Hydrophilic specific surface areas /m^2 g^{-1}			α (%)	m /μg cm^{-2}	S_{Pt-Ru} /m^2 g^{-1}
S	S_1	S_2	S	S_1	S_2			
Vulcan XC-72 carbon black as the support								
205	125	80	205	125	80	100	12	49
205	125	80	205	125	80	100	40	85
205	125	80	205	125	80	100	76	54
205	125	80	205	125	80	100	200	45
SWNT as the support								
465	125	340	104	74	30	22	12	85
465	125	340	104	74	30	22	27	85
465	125	340	104	74	30	22	80	83
465	125	340	104	74	30	22	230	61
$SWNT_f$ as the support								
100	52	48	121	64	57	121	4.1	362
100	52	48	121	64	57	121	5.5	255
100	52	48	121	64	57	121	6.9	166
100	52	48	121	64	57	121	9.7	138
100	52	48	121	64	57	121	18	105
100	52	48	121	64	57	121	29.5	39
100	52	48	121	64	57	121	52	37
100	52	48	121	64	57	121	66	76

Note. The following designations ae used: S is the total specific surface area, S_1 is the total specific surface area of mesopores, S_2 is the total specific surface areas of micropores, α is the surface fraction of hydrophilic pores, m is the amount of deposited Pt–Ru catalyst.

surface area of deposited Pt–Ru catalysts was determined based on the quantity of electricity consumed in the oxidation of adsorbed carbon monoxide. This method of determination of the surface area of platinum metals is well substantiated.[90,91] Note that the true surface area of Pt–Ru catalysts can be determined more accurately using the copper underpotential deposition (upd) procedure.[92,93] The specific surface area of a catalyst was determined by dividing its true surface area by the deposited amount of the catalyst.

By comparing the data on Pt–Ru catalysts deposited on Vulcan XC-72 and carbon nanotubes (see Table 3), the following conclusions can be drawn. The total specific surface area of $SWNT_f$ (measured with the use of octane) is much smaller than the surface area of original SWNT due to a substantial decrease in the micropore volume. Evidently, the surface groups situated at the ends of $SWNT_f$, prevent the access of octane molecules inside the nanotubes, which is confirmed by the BET data pointing to lower adsorption of nitrogen. Moreover, it is probable that surface groups can bind together neighbouring nanotubes into aggregates and thus partly block their external surface. This leads to a decrease in the mesopore surface. Due to functionalization, hydrophobic SWNT become hydrophilic. The porograms measured with the use of octane and water virtually coincide (see Fig. 14, curves *3* and *4*). The overall hydrophilic specific surface area of $SWNT_f$ exceeds that of original SWNT. The hydrophobicity of original SWNT is determined by the properties of graphene sheets that form their surface. The excess of the $SWNT_f$ hydrophilic specific surface area over total specific surface area can be explained by swelling of nanotubes in water.

Analysis of the data of Table 3 also showed that for very small catalyst weights (5–10 μg cm^{-2}) formed in the initial period of electrodeposition on $SWNT_f$, the specific surface areas may be very large, nearly 250 $m^2\ g^{-1}$ (particles measuring 1–2 nm). At the same time, this cannot be achieved by depositing the Pt–Ru catalyst on carbon black or original SWNT. Apparently, the electroplating on $SWNT_f$ produces much more catalyst metal nuclei per unit surface as compared with original SWNT or Vulcan XC-72. With the increase in the deposition time and the deposit weight, the specific surface area decreases and the size of particles increases on all supports. For the deposit weight of 10–12 μg cm^{-2}, the specific surface area of the $SWNT_f$-supported Pt–Ru catalyst remains 2–3 times greater as compared with the catalyst deposited on carbon black and original SWNT.

The tentative value (based on a TEM image) of the mean diameter of Pt–Ru particles deposited on $SWNT_f$ in an amount of 8.5 μg cm^{-2} with the specific surface area of 149 $m^2\ g^{-1}$ was found to be 2.3 nm. As the deposit weight increases to 70–80 μg cm^{-2}, the specific surface areas on different supports approach one another. Thus, it is only in the initial deposition stage that the support structure determines the degree of dispersion of the electroplated catalyst. For longer electroplating times, the deposit structure is determined by the deposition parameters.

The specific surface area of hydrophilic pores in $SWNT_f$ is not the highest in the series of supports; however, the particular structure of this material favours the formation of finer metal deposits. This is probably associated with its swelling when water molecules pull apart the hydrophilized nanotubes thus creating new micropores in which Pt–Ru nuclei can be formed. Localization of metal particles in micropores prevents their integration. The catalytic activity of deposited platinum catalysts (normalized per unit electroactive surface) was found[73–74] to be independent of the nature and properties of the support for catalyst amounts of 70–230 μg cm^{-2}. However, it turned out that on $SWNT_f$ one can obtain catalysts with high specific surface areas.

Step-by-step deposition of platinum on a porous titanium support was carried out.[38] During this process, the main maximum in differential porograms shifted to smaller sizes. This was explained by the deposition of platinum on the surface of coarse pores, which gradually decreases their size.

c. Electron-conducting polymers as catalyst supports

Attempts to use electron-conducting polymers, mainly polyanilines (PANI) as the supports for catalysts of methanol, formic acid and formaldehyde electrooxidation are described in the literature. The prospects of using such materials in FC were pinned on the enhancement of catalytic activity of polymer-supported platinum.[94–98] In individual cases, polymer degradation may occur if the optimal conditions of catalyst deposition have not been observed.[98] The use of electron-conducting polymers with deposited platinum group metals is considered as promising.[99–104] In connection with this, investigation of the porous structure of these polymers is important, because it can substantially affect the distribution of metal particles in the pores and, hence, the catalytic activity and electrochemical characteristics of FC. Detailed studies of the porous structure of PANI and poly-*p*-phenylene have revealed[105–108] their substantial swelling in water and other solvents. Figure 15 shows the integral porograms for PANI. The porous structure characteristics are substantially different for water and decane (the pore size in water is much larger). Since swelling is virtually absent in decane, the observed porous structure resembles that of dry PANI. Swelling of PANI in water is characterized by the formation of new fine pores with radii of only several tens of nanometres.

The structure of electron-conducting polymers substantially depends on the type of counter ions (*i.e.*, on the nature of emeraldine salt).[105–108] Emeraldine chloride was treated

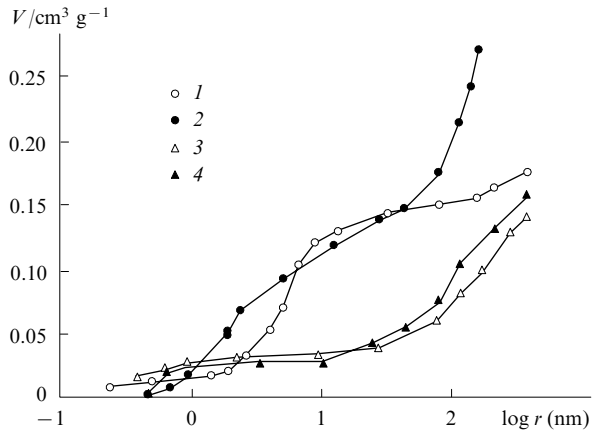


Figure 15. Integral porograms for polyanilines synthesized electrochemically (*1*, *3*) and chemically (*2*, *4*) recorded with the use of water (*1*, *2*) and decane (*3*, *4*).[105]

with various acids in order to replace chloride anions by other anions in the ion-exchange process.[105,106] Depending on the nature of the anion, the porosity varied from 0.59 $cm^3\ cm^{-3}$ (for BF_4^-) to virtually zero (for CF_3COO^-). As regards the degree of PANI swelling, the emeraldine salts under study can be divided into the following two groups:

— hydrophilic groups strongly swelled in water and water vapour (BF_4^-, $H_2PO_4^-$, Cl^-, HSO_4^-, $HCOO^-$);

— hydrophobic groups that remain virtually non-swelled in water ($CH_3C_6H_4SO_3^-$) or altogether refuse to be soaked in water (CF_3COO^-).

For emeraldine salts, Table 4 shows the values of hydrophilic porosity, hydrophilic specific surface area and average radius of individual PANI fibrils, which were calculated based on porosimetry data.[108] It is seen that for hydrophilic PANI salts, S_{phil} is very high, namely, varies from $\sim$400 to $\sim$600 $m^2\ g^{-1}$, *i.e.*, it is of the same order as S_{phil} of carbon supports (see above). The PANI structure in water is micro-mesoporous, like the structure of certain carbon supports. The integral porograms for all inorganic emeraldine salts exhibit an abrupt step at $r \approx 100$ nm and their porous structures differ mainly in the pore volume in this narrow region of radii.

Table 4. Hydrophilic specific surface area (S_{phil}), hydrophilic porosity (v_{phil}) and mean radius of individual fibrils (r_f) for PANI salts with different anions.[108]

Anion	S_{phil} /$m^2\ g^{-1}$	v_{phil} /$cm^3\ cm^{-3}$	r_f/nm
Cl^-	590	0.50	2.10
HSO_4^-	515	0.45	2.45
$H_2PO_4^-$	490	0.55	2.50
BF_4^-	470	0.60	2.70
$HCOO^-$	430	0.40	2.90
4-$MeC_6H_4SO_3^-$	$\sim$0	0.06	—
CF_3COO^-	0	0	—

It is interesting that in water, the porous structure of PANI substantially depends on the degree of its doping with chloride ions[108] and, hence, on the potential. This should be taken into account when considering the PANI performance in FC. Doping of the emeraldine base substantially increases the specific volume of pores (from 1.0 to 1.7 $cm^3\ g^{-1}$) and the specific surface area (from 310 to 520 $m^2\ g^{-1}$). The structures of emeraldine base synthesized from various precursors (emeraldine chloride, sulfate, phosphate) were found [109] to be different.

Hence, such factors as the lability of the PANI structure and the presence of nanosized (from 1 to 100 nm) pores favour the formation of platinum nanoparticles and their aggregation and provide high specific surface area. However, highly labile structures are probably prone to degradation induced by external factors.

d. Catalysts of solid oxide fuel cells

Characteristics of electrodes in FC with solid oxide electrolytes (solid-oxide FC, or SOFC) depend on their porous structure.[110] In theoretical studies [111–124] devoted to simulation of such electrodes, it was shown that electrochemical reactions proceed at the three-phase catalyst – solid electrolyte – pores interface, the gas reagent occurring in the pores. The experimental studies of the electrode porous layer involves the use of the BET method, measurements of ionic conductivity and SEM with mathematical analysis of images.[109,113–115] Conductivity measurements are important for elucidating the percolation effect, which is associated with the fact that the continuity of each of three phases can be broken in the case of its insufficient volume concentration in the electrode. A percolation theory of electrodes for solid oxide FC was developed.[125] It was shown that the dependence of the size of three-phase boundary on the porosity goes through a maximum. The standard contact porosimetry technique makes it possible to measure not only the porosity but also the interface size (see below).

The porous structure of the anode in solid oxide FC was studied by standard contact porosimetry and SEM.[126] The anode represented a cermet material built of fine powders of nickel and yttria-stabilized zirconia (YSZ) and provided sufficient ionic conductivity in the working temperature range of 900 – 1000 °C. The nickel catalyst was responsible for the high electron conductivity of the anode. Moreover, the anode contained an interconnected system of pores through which the gaseous hydrogen-based fuel was fed to the Ni/YSZ interface. According to the theory of porous electrodes, the electrochemical reaction proceeds at the three-phase Ni/YSZ/gas pores interface. This is why the main goal of studies was to determine the area of this interface. For hydrophilic gas-diffusion porous electrodes with liquid electrolyte, the three-phase intefacial area catalyst/liquid electrolyte/gas (S_s) was determined by integration of the porosimetric function $V(r)$ according to an expression analogous to Eqn (1). However, this method cannot be applied to electrodes in SOFC.

Based on the method of standard contact porosimetry, a technique for measuring S_s was developed for the mentioned case.[126] A $ZrO_2 + 8$ mass % Y_2O_3 anode was studied. First, with the use of octane, the porosimetric curve was measured for the original anode (Fig. 16). Then, nickel in the anode was dissolved in concentrated nitric acid, which was accompanied by the formation of new pores. Figure 17 shows the images of the anode surface before and after the removal of nickel. After washing and drying of the sample, its porogram (curve *2* in Fig. 16) was measured. In the region of $r < r_1$, pores were revealed which were absent in

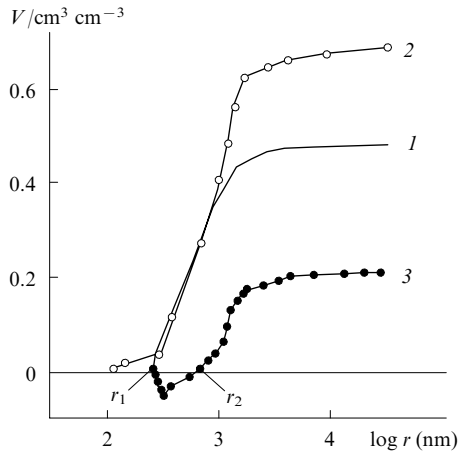


Figure 16. Integral porograms for the anode of a solid-oxide FC before (*1*) and after (*2*) removal of nickel particles (*3* is a difference curve).[126]

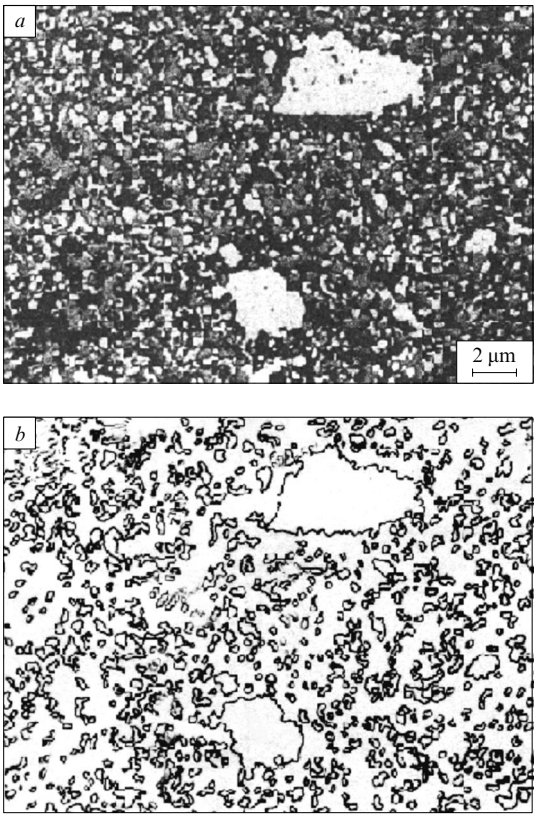


Figure 17. Anode surfaces originally (*a*) and after the removal of nickel (*b*).[126]
White areas are pores, grey areas are nickel agglomerates and black areas are electrolyte particles.

the original sample. These pores appear after the removal of fine nickel particles embedded into coarser electrolyte particles with the volume $V_1(r_1)$ and make no contribution to the target three-phase surface S_s because they do not contact the coarser gas pores. Figure 18 illustrates the porous anodic layer. In the region of small r, the V values are negative (see curve *3* in Fig. 16). They correspond to pores located inside nickel agglomerates and between individual nickel particles and also make no contribution to S_s (due to the absence of contact with electrolyte particles).

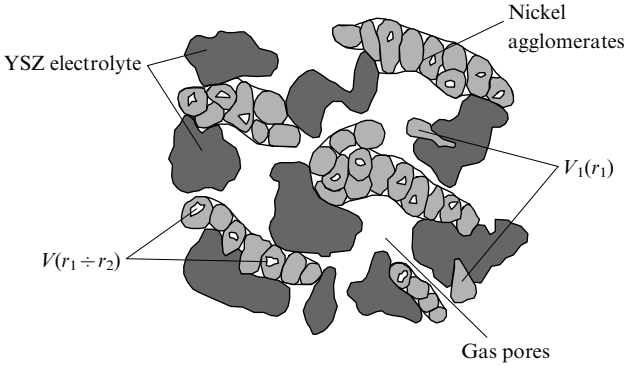


Figure 18. Illustration of the anode structure.[126]

The pores contributing to S_s have $r > r_2$. The magnitude of S_s is found based on an expression analogous to expression (1).

The thus calculated total three-phase interfacial area Ni/electrolyte/gas pores is determined by the surface area of pores with radii $r > r_2$; moreover, it is contributed by not only agglomerates but also individual nickel particles. The magnitude of S_s for all studied samples was in the range from 0.98 to 1.24 $m^2\ cm^{-3}$. The mathematical processing of SEM images (see Fig. 17) allowed the number of contacts (N) on the three-phase interface to be calculated. For different electrodes (original and aged), this value fitted the range from 1.5×10^6 to 3.4×10^{10} and was proportional to S_s. The exchange current density for various electrodes was found to be proportional to S_s and N. Thus, S_s was shown to correspond to the electroactive specific surface area which can be used in calculations of the hydrogen oxidation kinetics.

3. Gas-diffusion layer

The anodic and cathodic gas-diffusion layers involved in the membrane-electrode assembly are adjacent to the catalytic electrode layers. They play a very important role in proton-exchange membrane FC (PEMFC),[1–3] particularly, they protect thin and labile catalytic layers from mechanical impacts from gauze metal current terminals. In the pores of gas-diffusion layer, processes of two types occur: the transport of active gases (oxygen, hydrogen) by gas-permeable pores to catalysts and the transfer of water vapour in the opposite direction; the transport of water by liquid-permeable pores from the catalytic layer (as a rule, from the cathode) to the gas chamber.[127–141] Hence, the gas-diffusion layer should have sufficient volumes of both hydrophobic and hydrophilic pores. Its second function is electron conduction, because it conducts current from the membrane-electrode assembly to the metal gauze terminals. This is why the matrix of the gas-diffusion layer is prepared on the basis of carbon paper or carbon cloth,[1,2] *i.e.*, porous materials with hydrophilic and hydrophobic pores. However, insofar as their hydrophobic properties are insufficient, they are additionally hydrophobized with fluoropolymers and, sometimes, carbon black.

It is evident that the hydrophilic-hydrophobic properties and the porous structure of gas-diffusion layers have a substantial effect on proton-exchange membrane FC characteristics.[1–3,142,143] Nonetheless, the information on hydrophilic-hydrophobic properties of the gas-diffusion layer is scarce. Some effective contact angles of gas diffusion layers were reported to be determined.[24,31] This was done by the well-known Washburn method[23] by measuring the rate of water (or other liquid) rise inside porous layers. This method can be directly applied only to hydrophilic materials with water wetting contact angles of $< 90^\circ$, whereas the mean angle is $> 90^\circ$ for the majority of layers. This is why to obtain the desired quantity as applied to water, the authors of the above studies resorted to approximate extrapolations based on experimental values of contact angles $\theta < 90^\circ$ for various wetting liquids with the known coefficients of surface tension.[24,26–31]

To assess the rates of transfer of water vapour and water in gas-diffusion layers, one must know the size of pores where these processes occur. However, even the refined Washburn method fails to provide this information. To solve this problem, the method of standard contact poros-

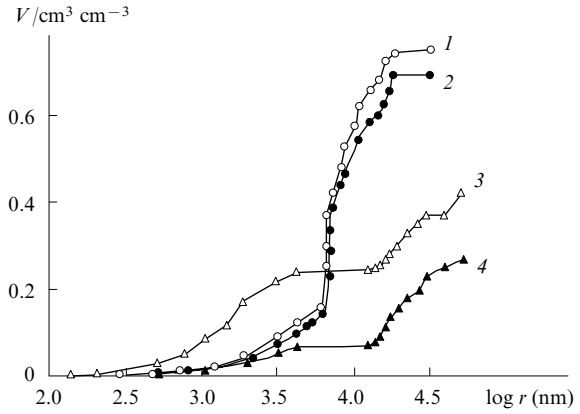


Figure 19. Integral porograms for original (*1*, *3*) and hydrophobized (*2*, *4*) carbon paper Toray measured with the use of octane (*1*, *2*) and water (*3*, *4*).[144]

imetry was used recently.[144, 145] The Toray carbon paper, both original and hydrophobized at various fluoropolymer concentrations was studied.[144] Figure 19 shows the integral curves of pore volume distribution *versus* effective radius (r^*) measured using octane and water for the original carbon paper and the corresponding gas-diffusion layer containing 27 mass % of the fluoropolymer. From the curves measured in octane, it is evident that the porous structure of original paper is monodisperse (with pore radii varying from 10 to 30 μm) with very high overall porosity (~0.75). After the treatment with a PTFE suspension, the total porosity somewhat decreased. Due to poorer wetting with water, the r^* values in curves *3* and *4* were expected to shift. However, this was observed only for porograms of paper samples with sufficiently high PTFE contents. For paper samples containing no additives, the porosity was observed to increase in the range of fine pores with $r < 3$ μm. This is explained by swelling of fibres that form the fine pores with high surface area. The swelling of materials is favoured by their high porosity (in this case, ~0.75) when the porous structure is not strong. In the presence of PTFE, the sorption of water and the degree of swelling decrease.

Table 5 shows the total, hydrophilic and hydrophobic porosity values for clean paper of the Toray type and also for its two samples with different PTFE concentrations (c_f), which were determined based on porograms. For a gas-diffusion layer with c_f of 18 mass % and 27 mass %, the hydrophilic and hydrophobic porosity values are close to one another.

Table 5. Total (υ), hydrophilic (υ_{phil}) and hydrophobic (υ_{phob}) porosity ($cm^3\ cm^{-3}$) of carbon paper Toray before and after hydrophobization.

Paper	υ	υ_{phil}	υ_{phob}	λ (see [a])
Carbon paper Toray	0.75	0.42	0.33	–
Toray + 18 mass % PTFE	0.70	0.29	0.41	2.3
Toray + 27 mass % PTFE	0.69	0.27	0.42	1.6

[a] Hydrophobization efficiency.

The concept of hydrophobization efficiency (λ) of the porous carbon matrix of gas-diffusion layer [the ratio of hydrophobic porosity (vol.%) to the PTFE concentration (vol.%)] was introduced.[144] The real densities of fluoropolymer and carbon materials are similar; hence, in the first approximation, the fluoropolymer concentration in volume percent can be equated to its concentration in mass percents. The concept of hydrophobization efficiency was introduced because for the gas-diffusion layer in a proton-exchange membrane FC, it is important to know what fluorplastic concentration was used to achieve one and the same hydrophobic porosity. The higher c_f the higher the electric resistance of the gas-diffusion layer, because fluoropolymer is an insulator. The hydrophobization efficiency for $c_f > 18$ mass % substantially decreases (see Table 5). Probably, for low c_f values, the fluoropolymer particles are mainly deposited on the carbon support, whereas for high concentrations, the deposition proceeds on already deposited polymer particles. In the latter case, the hydrophobic porosity remains virtually unchanged with the increase in the fluoropolymer concentration. Besides the suspension of F-4D fluoropolymer, which was used for all gas-diffusion layer samples described above, a suspension of FEP 121A fluoropolymer was used.[144] Based on the porograms for a gas-diffusion layer with $c_f = 15$ mass %, the hydrophilic and hydrophobic porosity values were assessed to be 0.22 and 0.51, respectively. Hence, $\lambda = 3.4$, which is substantially higher than λ for a layer with the F-4D fluoropolymer. This can be explained by different compositions and structures of molecules in these fluoropolymers: F-4D (PTFE) has the $(-CF_2-CF_2-)_n$ structure while FEP121A has the $(-CF_2-CF(CF_3)-CF_2-)_n$ structure that contains hydrophobic CF_3 groups in addition to CF_2 groups.

To model the performance of a gas-diffusion layer in PEMFC, it is important to know the dependences of the water wetting contact angle of the pore surface (θ) on the pore radius (the flow rate of water generated in the catalytic layer through the gas-diffusion layer is determined by both the pore radius and θ). These dependences for the gas-diffusion layer based on Toray carbon paper hydrophobized by various fluoropolymers were recorded by standard contact porosimetry.[144] Figure 20 shows the dependences of the contact angle of hydrophilic pores on their radius, which

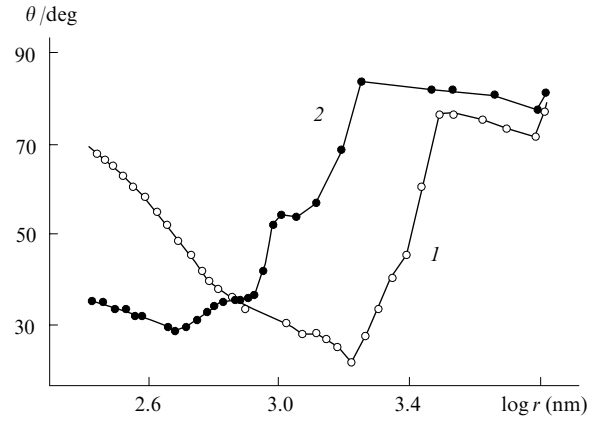


Figure 20. Dependences of the contact wetting angle of carbon paper Toray containing 27 mass % of PTFE deposited from F-4D (*1*) and FEP 121A (*2*) suspensions.[144]

were calculated based on the corresponding porograms measured with the use of octane and water for a gas-diffusion layer containing 27 mass % of fluoropolymer deposited from F-4D and FEP 121A suspensions. Both dependences have minima.

The non-uniform wetting of different pores with water is explained by the non-uniform distribution of fluoropolymer particles and surface groups over pores of different size. It is evident that owing to their size, the fluoropolymer particles cannot fit very fine pores. This is why the surface fraction of fluoropolymer-occupied pores with radius r is $\rho(r) = 0$ and $\theta(r) = \theta_{carbon}(r) < 90^\circ$. The walls of very coarse pores are completely covered with fluoropolymer particles for sufficiently high concentrations of the latter. Thus for these pores, $\rho(r) = 1$ and $\theta(r) = \theta_f > 90^\circ$, which means that they are hydrophobic. In pores with medium radii, $0 < \rho(r) < 1$ and $\theta_{carbon}(r) < \theta(r) < \theta_f$. The ascending branch in each of curves under discussion shows that as the pore radius increases, more fluoropolymer particles are deposited. The descending branch in the range of fine pores corresponds to the non-uniform distribution of hydrophilic surface groups. In this size interval, as the pore size increases, the concentration of hydrophilic surface groups apparently increases.

The rate of water penetration into the gas-diffusion layer and its distribution throughout the layer thickness were estimated according to the well-known Darcy equation and based on the data on mean contact angles.[3] These data are important when simulating the performance of a PEMFC with the water removal from the membrane-electrode assembly through the gas-diffusion layer. However, the validity of these calculations could have been higher if the aforementioned $\theta(r)$ dependences had been taken into account.

As a finely disperse hydrophobic layer containing particles of PTFE and Pureblack carbon black has been deposited onto carbon paper, the required hydrophobization of the latter occurs. In the process, besides coarse pores with diameters from $\sim$10 to 200 μm, the finer pores of the hydrophobic layer with diameters from $\sim$0.01 to 1 μm are formed in this system,[128,146] as follows from the differential curve of pore volume distribution *versus* diameters measured by mercury porosimetry (Fig. 21). Similar results were obtained in another study.[146] However, it should be borne in mind that intrusion of mercury under pressure of several hundred kPa into so soft material with very high porosity (0.75–0.78) inevitably leads to distortion of the porosimetric curve.

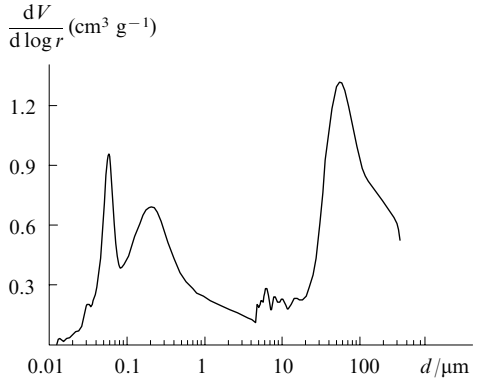


Figure 21. Differential curve of pore volume distribution *versus* diameters for a gas-diffusion layer supported on carbon paper coated by a hydrophobized layer consisting of PTFE particles and Pureblack carbon black.[128]

IV. Membranes

Polymeric ion-exchange membranes or electrolyte-containing capillary inorganic membranes are the key components of FC.[1] Ion-exchange membranes are used in electrodialysis and electrolysis, whereas inorganic electrolyte-containing membranes are used in electrolyzers and sensors. The functional role of membranes is to provide ionic conduction and prevent short-circuiting of electrodes. The method of standard contact porosimetry is very convenient for studying the porous structure and the sorption and capillary properties of all membranes,[35–37] because it allows one to specify particular compression pressures and temperatures and, if necessary, to use FC electrolytes as the measuring liquids.

1. Capillary membranes

Capillary membranes are used in FC with alkaline and phosphoric-acid electrolytes. The porous structure of chrysotile asbestos, which is widely used in electrochemical devices (FC, electrolyzers, *etc.*) with alkaline electrolytes, was studied.[35,36] Octane (σ = 21.75 mN m^{-1}), water (σ = 72.75 mNH m^{-1}) and 7 M KOH solution (σ = 92 mN m^{-1}) were used as the measuring liquids. For alkaline (or other) electrolyte, methods of evaporation and condensation cannot be used to change the liquid quantity; therefore, capillary impregnation and capillary suction were used. In the first case, the dry sample to be studied is brought into contact with several standard samples soaked in different amounts of liquid. In the second case, the completely soaked sample is brought into contact with dry standard samples. Figure 22 shows the corresponding differential porograms.

In octane (curve *1*), chrysotile asbestos remains virtually non-soaked and the porogram characterizes its natural porous structure. In water (curve *2*), asbestos is soaked, which gives rise to micropores with radii varying from 10^3 to 4.5×10^4 nm. In alkaline solutions (curve *3*), the pore volume is observed to further increase in the region of

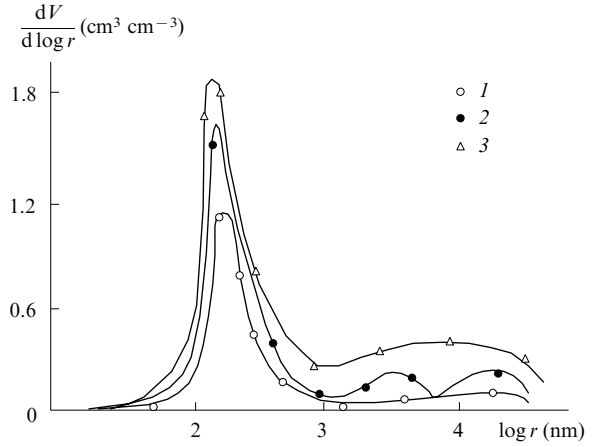


Figure 22. Differential porograms for chrysotile asbestos measured with the use of octane (*1*), water (*2*) and 7 M KOH solution (*3*).[36]

coarse pores. The degree of soaking of chrysotile asbestos increases with the increase in the surface tension of liquid due to the increase in the capillary pressure in the pores [see Eqn (2)]. The appearance of very coarse pores in the swelled membrane may play the crucial role because the active gases (O_2 and H_2) can be mixed in the pores when the total electrolyte volume in the membrane-electrode assembly is insufficient. In this case, explosive mixtures can be formed and emergency conditions can occur. It deserves mention that the total electrolyte volume in the membrane-electrode assembly depends on the heat and mass exchange processes in the FC (for details, see Ref. 147).

2. Ion-exchange membranes

In ion-exchange membranes, the ionic conduction is performed by labile counter-ions of the polymer functional groups.[45] In the dry state, ion-exchange membranes exhibit nearly zero ionic conductivity; however, conductivity appears upon soaking with water due to lability of counter-ions. As the moisture content increases, the conductivity also increases up to a certain limit. Due to substantial swelling of membranes in water, their porous structure in the working state is studied by the method of standard contact porosimetry with the use of water as the measuring liquid.

a. Homogeneous ion-exchange membranes

Homogeneous ion-exchange membranes (solid polymer electrolytes) contain only one phase of water-soaked ionomer. Such membranes are widely used in proton-exchange membrane FC and for FC with direct methanol oxidation and also in electrodialysis cells. Figure 23 shows differential porograms for an anion-exchange homogeneous membrane MA-100 measured with the use of octane and water. Upon contact with octane, virtually no pores are formed in the membrane, because it does not swell in octane. Membrane exposure to water gives rise to fine pores with the radius of 510 nm. The well-known proton-exchange perfluorinated sulfocationic membranes of the Nafion type, which contain hydrated polyperfluorosulfonic acid as the ionomer, can serve as examples of homogeneous ion-exchange membranes.

Pores in these membranes appear only upon their exposure to water due to hydration of ion-exchange

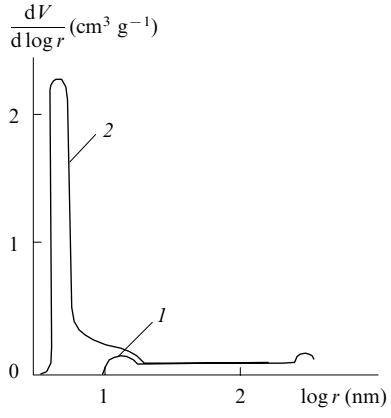


Figure 23. Differential porograms of MA-100 membrane, measured with the use of octane (*1*) and water (*2*).[148]

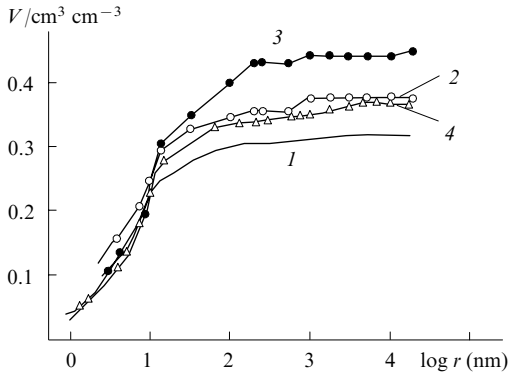


Figure 24. Integral porograms for membranes MF-4SK (*1*), Nafion 112 (*2*), Nafion 115 (*3*) and Nafion 117 (*4*), measured with the use of water.[150]

groups[149] (water molecules pull the polymer chains apart). Upon their exposure to octane and other hydrocarbons, pores are virtually absent, as in dry membranes. Figure 24 shows the integral porograms of Nafion 112, Nafion 115 and Nafion 117 ionomers and of their Russian analogue MF-4SK, measured with the use of water.[150] The main pore volume refers to micro- and mesopores with $r < 10$ nm. Such membrane structure is called the microstructure or the 'ion exchanger phase'. In the region of small pore size, the porograms of all membranes are very similar. In our opinion, this means that the microstructure is determined by the chemical nature of membranes, which is the same in this case. Taking into account the results of several other studies of other brands of ion-exchange membranes, this conclusion can be taken as general for ion-exchange membranes. In the pore size range of $10 < r < 500$ nm, the curves in Fig. 24 differ for different membranes, their deviations being determined by the contribution of coarse pores to the total porosity.

Apparently, technological defects are specific for each membrane brand. The small volume of the coarsest pores with $r > 500$ nm is associated with the roughness of the membrane external surface, as confirmed by the data of microscopic studies. Based on measurements with the use of water and octane, it was concluded that these pores are hydrophobic. This can only be explained by the orientation of surface sulfo groups inwards the membrane due to cohesion, which agrees with the results of another study[45] in which the hydrophobicity of the Nafion-type membrane surface was established upon measurements of its contact angle with water (see also the conclusions drawn in Section III.1.b on the inversion of ion-exchange groups with respect to the polymer chain, see Fig. 6).

It was shown[149] that any modification in the membrane preparation method affects the porous structure. For instance, the increase in the exchange capacity of MF-4SK membranes from 0.71 to 1.02 mg-equiv g^{-1} almost doubled their porosity in water. The effect of different liquids on the porous structure of Nafion type membranes was studied.[149] The total volume of micro- and mesopores in ethanol was found to be almost twice that in water (this should be borne in mind when analyzing the performance of ethanol–air FC). The degree of swelling of ion-exchange membranes depends on the nature of counter-ions. For MF-4SK membranes, the substitution of sodium ions Na^+ for pro-

tons decreased the porosity by 30%. The membrane pore volume is substantially reduced upon the substitution of inorganic counter-ions for organic ions.

b. Heterogeneous ion-exchange membranes

Heterogeneous membranes contain ion-exchange components in addition to the ion exchanger phase. As an example, Fig. 25 shows the differential porograms for heterogeneous cation-exchange membranes MK-40 prepared by co-polymerization of styrene and divinylbenzene (DVB). Membranes with different DVB contents were studied.[151] As the binder, polyethylene was added into the heterogeneous membrane compositions. All curves in Fig. 25 have two maxima, one the region of micro- and mesopores with the radii from <1 nm to ~ 100 nm (microstructure) and one in the region of macropores with the radii from ~ 300 to 3000 nm. The pores of the first type are formed due to ion exchanger phase swelling, and the second type pores are formed by the inert polyethylene phase. An increase in the DMB content induced a decrease in the first peak and an increase in the second peak.

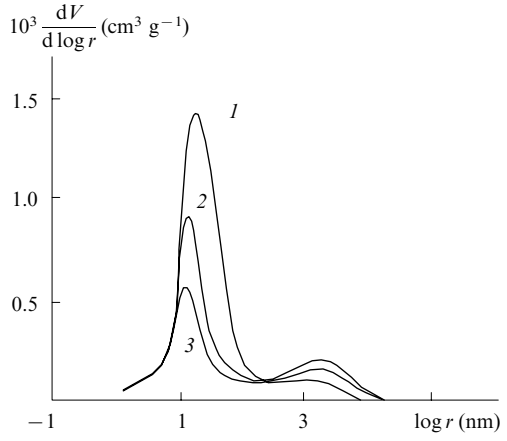


Figure 25. Differential porograms for heterogeneous membranes MK-40 containing 2 mass % (*1*), 4 mass % (*2*) and 8 mass % (*3*) DVB, measured with the use of water.[151]

Thus, the ratio of the total volume of micro- and mesopores to the total volume of all membrane pores makes it possible to assess the degree of its true homogeneity. Based on numerous data, it can be concluded that swelling in water affords micro- and mesopores in polymer ion-exchange membranes and mainly gives rise to formation of additional macropores in inorganic capillary membranes.[37, 38, 54, 151]

3. Composite membranes

Polymer fibrous composites are sometimes used as ion-exchange materials. The combination of different types of fibrous fillers with ion-exchange matrices furnishes materials with a wide range of characteristics. Cation-exchange chemisorption composite fibre membranes Polycon are obtained by the polycondensation inflation method as follows. The sulfonated phenol cation exchange matrix is synthesized on the surface and in the bulk of polyacrylonitrile fibre filler by applying the monomer solution on it followed by pressing. The pressing is accompanied by the internal exothermal heating of the material, which affects the resulting membrane structure.

The porous structure and the sorption and hydrophilic-hydrophobic properties of these membranes formed at various compression pressures were studied.[47] As the measuring liquids for standard contact porosimetry, water and octane were used. Porograms and contact angle *vs.* pore radius dependences were measured. It was found that the structure of Polycon membranes is sufficiently complex and in its water-swelled state includes both the porous structure of fibres and the structure of swelled disperse ion exchanger phase with pores filled with water. In the general case, the fibres contain hydrophilic micropores with the contact angle $\theta \approx 0^\circ$, hydrophilic-hydrophobic mesopores with $\theta < 90^\circ$ and hydrophobic meso- and macropores with $\theta > 90^\circ$. The ion exchanger phase contains only completely hydrophilic ($\theta \approx 0^\circ$) micro- and mesopores. Measurements of the specific surface areas for both phases by standard contact porosimetry have shown that for different versions of Polycon membrane with the same ion exchanger phase mass fractions (0.9), the specific surface areas can differ by a factor of almost seven (70 and 480 m^2 g^{-1}). However, the exchange capacity of all membranes was virtually the same, namely, 2.6 – 2.8 mg-equiv g^{-1}. These results can be explained by different orientations of ion-exchange groups with respect to the polymer chain and, correspondingly, different distribution of water molecules in the membrane bulk. Hence, water molecules determine the ion exchanger structure during the hydration process and the size of ion-exchange clusters.

Thus, by varying the compression pressure in the synthesis of Polycon membranes, one can change the orientation of ion-exchange groups with respect to the polymer chains. This confirms once again the described[43] phenomenon of the inversion of ion-exchange groups with respect to the polymer chain (see Section III.1.b). This behaviour was also observed for various ion-exchange groups and different polymer chains;[44, 47] this is why we believe that it is common for ion-exchange membranes and resins.

The porous structure of a composite capillary membrane in medium-temperature FC with phosphoric-acid electrolyte was studied.[54] Membranes were prepared by mixing together the silicon carbide and PTFE powders in the ratio of 9 : 1 followed by pressing and sintering. Experiments were carried out with the use of decane and water. These matrices were strong and did not swell in water or electrolytes. The use of water as a measuring fluid was dictated by the necessity of studying the hydrophilic-hydrophobic properties of the membrane. The volume fraction of hydrophilic pores was $\sim 90\%$, the radius of most pores fitted the range of 10 – 80 nm, the overall range being from 0.01 to 50 μm.

4. Pore corrugation in membranes

In the studies of ion-exchange membranes, keen attention is paid to corrugation of the pores. In this aspect, the homogeneous anion-exchange membrane MA-100 and pilot (laboratory-made) heterogeneous ation-exchange membranes with carboxyl ion-exchange groups were studied.[148] Pilot membranes were prepared by copolymerization of methacrylic acid (MAA) with divinylbenzene in a polyethylene (PE) solution in *m*-xylene. Figure 26 shows the integral energy isotherms for water adsorption and desorption (in $v-A$ coordinates); the integral porogram measured in the course of decane evaporation (in $V-r$ coordinates);

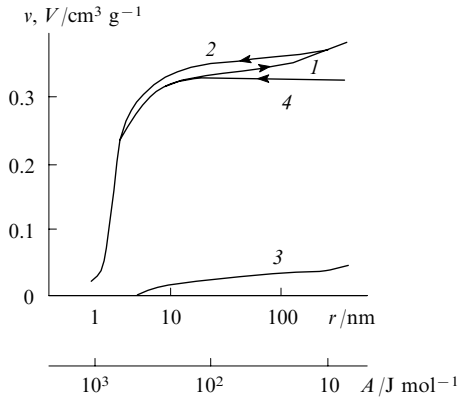


Figure 26. Integral energy isotherms of water adsorption (*1*) and desorption (*2*); an integral porogram measured with the use of decane (*3*) and the difference (*2*−*3*) curve (*4*) for MA-100 membrane.[148]

and the difference porogram obtained by subtracting the decane specific volume from the water specific volume at r = const for MA-100 membrane. It can be seen that in the course of soaking in water, the total pore volume increases by an order of magnitude; moreover, only nanosized pores are formed; the structure of coarse pores remains virtually unchanged as compared with the dry membrane. The adsorption and desorption curves of the water-swelled membrane completely coincide in the region of microstructure; in the macrostructure region, a small hysteresis is observed.

Figure 27 shows the analogous family of curves for a pilot heterogeneous membrane of the MAK/DVB/PE type. In this case too, complete coincidence of adsorption and desorption curves of water-swelled membrane is observed in the microstructure region and a hysteresis appears in the macrostructure region, which is much wider than the hysteresis observed for the homogeneous (more accurately, quasi-homogeneous) membrane MA-100. This conclusion concerns all the membranes dealt with in the aforementioned publication.[148]

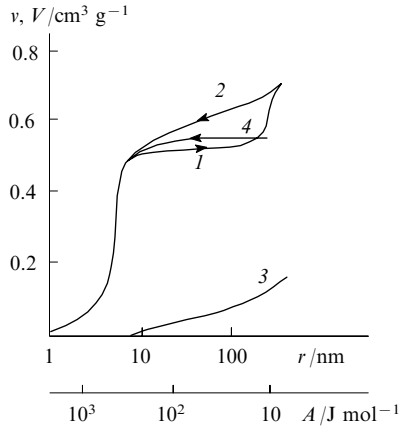


Figure 27. Integral energy isotherms of water adsorption (*1*) and desorption (*2*); an integral program measured with the use of decane (*3*) and difference (*2*−*3*) curve (*4*) for a heterogeneous membrane of the MAK/DVB/PE type.[148]

Thus, the pores formed upon swelling in water are not corrugate, whereas macropores in the heterogeneous structure are corrugate. Insofar as corrugation enhances the pore tortuosity, the homogeneous membranes that virtually lack macropores should exhibit the highest effective values of conductivity and diffusivity. We assume that this conclusion is common for all ion-exchange membranes. In particular, it explains the very high conductivity of Nafion membranes.

5. The effect of compression pressure and temperature on the porous structure of membranes

Studying how the compression pressure affects the structure of a MA-100 membrane has shown [148] that an increase in the pressure induces an decrease in porosity because the volume of the coarsest pores decreases while the structure of micro- and mesopores remains unchanged. As the pressure increases further, the volume of progressively smaller pores decreases.

The possibility of studying the porous structure of membranes at different temperatures is important because this provides data on the membrane structure for the working temperature of proton-exchange membrane FC. The porous structure of a water-swelled Nafion 117 membrane was studied [150] at room (20 °C) and working (80 °C) temperatures. A temperature rise was found to reduce the volume of pores with radii >10 nm.

6. Isotherms of capillary pressure and water desorption

The knowledge of capillary pressure isotherms for membranes is important for optimization of working conditions for proton-exchange membrane FC and simulation of their voltammetric characteristics. Particularly, the high capillary pressure prevents a membrane from excessive drying near the anode at high current densities, and this is beneficial for voltammetric characteristics.[152] Capillary pressure isotherms were measured [148] for different versions of Nafion membranes. Figure 28 exemplifies such isotherms for Nafion-117 at 20 and 80 °C.

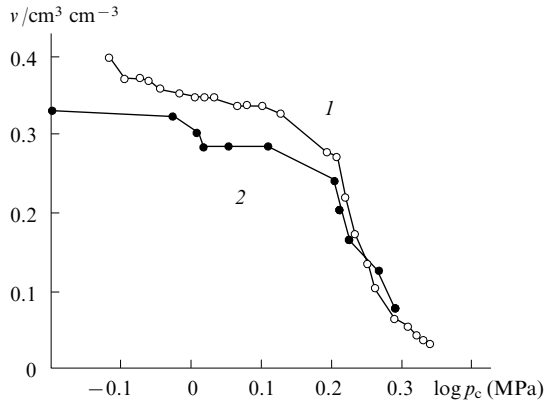


Figure 28. Integral capillary pressure isotherms for Nafion 117 membrane at 20 (*1*) and 80 °C (*2*).[148]

Figure 29 shows the isotherms of water desorption [$v\,(p/p_s)$ curves] for Nafion 117 at 20 and 80 °C. The p/p_s coordinate was calculated using Eqn (7). The membrane-

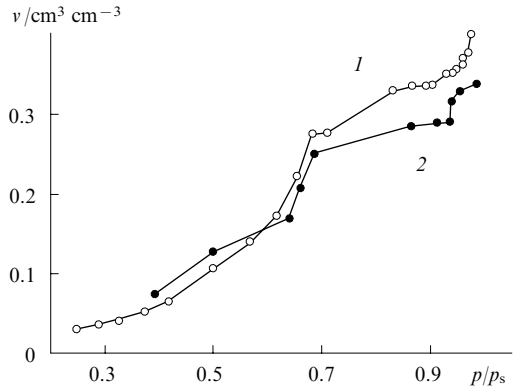


Figure 29. Integral isotherms of water desorption for Nafion 117 membrane at 20 (*1*) and 80 °C (*2*).[150]

electrode assembly in FC adjoins the anodic and cathodic gas chambers; hence, it is important to know the isotherms of water desorption (adsorption). The relative humidity (p/p_s) in the chambers varies depending on heat and mass exchange conditions in the FC. If the p/p_s ratio in the gas chamber is lower than in the membrane, then water evaporates from the membrane-electrode assembly to this chamber and *vice versa*. At the same time, the water content in the membrane and in the assembly substantially affects the electrochemical characteristics of FC,[152] mainly due to the strong dependence of the membrane conductivity on its water content. Thus as the ratio p/p_s decreases from 1 to 0.8, the quantity v for membrane at 80 °C decreases by 20% (see Fig. 29), inducing a decrease in the FC electrochemical characteristics (its power at different current densities).

V. The effect of the porous structure of membrane-electrode assembly components on the electrochemical characteristics of fuel cells. Optimization of the porous structure

1. Catalytic layer

A catalytic layer (or a gas-diffusion electrode) represents a system of two interpenetrating continuous masses of random configuration,[153–156] where the first mass is the catalyst (and support) flooded with electrolyte solution (microstructure) and the second continuous mass is formed by a system of wide gas pores or, in hydrophobized electrodes, by agglomerates of hydrophobic particles with gas pores in between. The most important characteristic of the catalytic layer is the specific interfacial area (S_x) between these masses. In hydrophilic catalytic layers, the S_x value is determined by integration of the pore volume distribution function *versus* radius for pores free of liquid. This value can be found based on an equation analogous to (1). In hydrophobic catalytic layers (in contrast to hydrophilic layers), the volume of pores free of liquid is constant and S_x is measured by standard contact porosimetry with the use of water and octane.[53]

The catalytic layer is a system with doubly distributed parameters, namely, along coordinate x coinciding with electrode thickness (macrostructure) and along coordinate y oriented normally to the interface formed between the electrolyte-flooded catalyst agglomerates and the gas pores (microstructure).[111–115, 153–160] In the catalytic layer, the gas–liquid electrochemical reaction of oxygen reduction or hydrogen oxidation occurs. The active gas (O_2 or H_2) is quickly transported through gas pores of the macrostructure and dissolved in electrolyte (in hydrophilic pores) near their interface with the microstructure. Then, the dissolved gas diffuses through the microstructure bulk to the catalyst surface on which the electrochemical reaction occurs.

The equation for steady-state diffusion of dissolved gas is as follows:

$$\frac{d^2c}{dy^2} = -\frac{S}{nFD}\,i\,(\eta, c), \tag{10}$$

where c is the dissolved gas concentration; S is the specific surface area of the catalyst per unit of its flooded mass; i is the local current density per unit of the catalyst true surface; η and $\varphi = \alpha\eta F/RT$ are the dimension and dimensionless polarization values; α is the transfer coefficient of the reaction slow stage; n is the number of electrons involved in the reaction; F is the Faraday number; D is the effective diffusion coefficient of the dissolved gaseous reagent.

When modelling the macrokinetics of gas-liquid reactions, the macrokinetic Butler–Volmer relationship[109, 161–165] is conventionally used

$$i = i_0\left\{\exp\frac{\alpha F}{RT}\,\eta - \exp\left[-\frac{(1-\alpha)F}{RT}\,\eta\right]\right\}, \tag{11}$$

where i_0 is the exchange current density per unit catalyst true surface.

It should be noted that relationship (11) is simplified and, hence, it ignores the multistep character of the reaction and peculiarities of the rate-limiting step kinetics. The phenomenological coefficient α in a wide interval of η is not necessarily constant.[51] Solution of the system of equations (10), (11) with boundary conditions affords, for $\alpha = 0.5$, the following expression for integral (differential) current density (I_d) related to unit interfacial area

$$I_d = -nFD\left.\frac{dc}{dy}\right|_{y=0} = \frac{nFDc_0}{l_d^0}e^{\varphi/2}(1-e^{-2\varphi})\,\mathrm{th}\left(\frac{l}{l_d^0}e^{\varphi/2}\right), \tag{12}$$

where $l_d^0 = \sqrt{nFDc_0/i_0S}$ is the characteristic diffusion length, $l = C_v/S_x$ is the half-thickness of the microstructure, C_v is the volume fraction of the flooded catalyst mass.

Taking into account that I_d, *i.e.*, the integral current density for microstructure, is at the same time the local current density for macrostructure (per unit external surface of the macrostructure), the following expression was derived for the potential distribution over the catalytic layer thickness:

$$\frac{d^2\eta}{dx^2} = \frac{d^2\varphi}{dX^2}\,\frac{RT/\alpha F}{l_{om}^2} = -\frac{S_xI}{k^*}, \tag{13}$$

where $X = x/l_{om}$ is the dimensionless coordinate, l_{om} is the characteristic ohmic length, $k^* = k\upsilon^2$ is the electrolyte effective conductivity in catalyst pores, k is the electrolyte conductivity, υ is the porosity, I is the overall current density.

As can be seen from these equations, the electrochemical characteristics of catalysts substantially depend on their porous structure, *i.e.*, on the pore volume distribution *versus* pore radius, porosity, and specific surface area.

In several studies,[56, 154, 155] the electrochemical curves of flooding, *i.e.*, the dependences of the polarization at different current densities (I) on the degree of catalyst flooding (ω) with electrolyte (ω is the ratio of flooded pores to the total pore volume), were calculated by numerical methods for some types of porograms. It was shown that in the first approximation, these curves have a single minimum (see curve *2* in Fig. 30). In the region of small ω, the increase in polarization is caused by ohmic loss of energy in the macrostructure due to low k*, whereas for large ω, the higher polarization values are caused by the active gas diffusion rate in the microstructure. Thus, the minimum polarization values and hence the minimum energy losses are observed in the region of medium ω. It was shown [53] that experimental electrochemical curves of flooding well agree with curves calculated according to the system of equations shown above. Based on the calculated electrochemical curves of flooding, it is possible to find the interval of optimal electrolyte content in the vicinity of the minimum in these curves.

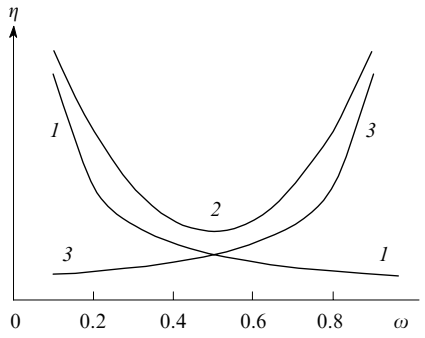


Figure 30. Schematic electrochemical curves of flooding for membrane (*1*), catalytic layer (*2*) and gas-diffusion layer (*3*) of a hydrogen–oxygen FC.

2. Ion-exchange membrane

One of the problems faced by scientists is the aforementioned 'water management'. This implies taking into account the dependence of voltammetric characteristics on the water transport both inside and outside the membrane when water is removed from a FC in which it is being generated.[150, 152] In fuel cells with proton-conducting Nafion membranes, water is generated on the oxygen electrode (cathode) and protons are generated on the hydrogen electrode (anode) to be consumed on the cathode (Fig. 31). When transferred from the anode through the membrane, protons carry along a certain amount of water molecules by the electroosmosis mechanism. As a result, the degree of flooding of membrane pores turns out to be higher on the cathodic side of the membrane than on its anodic side. Hence, the border between flooded and dry pores is located at larger pore radius on the cathodic side of the membrane than on the anodic side. Insofar as the capillary pressure (p_c) equal to the pressure difference between the gas (p_g) and liquid (p_l) phases on both sides of the meniscus

$$p_c = p_g - p_l , \tag{14}$$

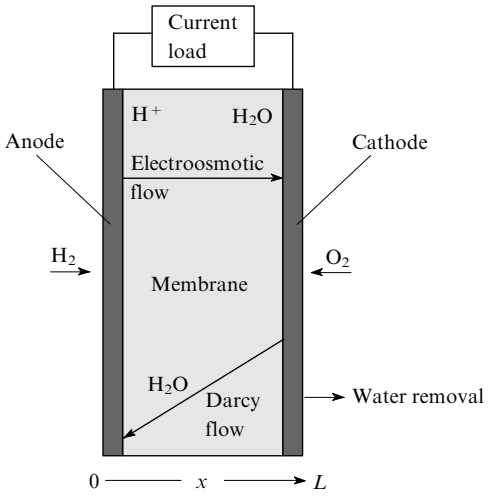


Figure 31. Illustration of water and proton flows in the ion-exchange membrane of a proton-exchange membrane FC.

is, according to the Laplace law, inversely proportional to the pore radius, then $p_c^a > p_c^c$ (the superscripts a and c correspond to anode and cathode, respectively). This is why after switching on the current, the water pressure on the cathodic side is first higher than on the anodic side. Due to the capillary pressure difference, the water flow is directed from cathode to anode. Under steady-state conditions, both water flows are equal; however, in this state, the moisture content (v) on the anodic side of the membrane turns out to be smaller than on the cathodic side. The local values of v_x, p_{cx} , p_{lx} depend on coordinate x along the membrane thickness, as well as the threshold pore radius (r_x) between the gas and flooded pores. The equation for the water flow through the membrane related to unit external surface (j_m) has the form [152, 163]

$$j_m = n_w j_p - c_w \frac{K(v_x)}{\mu} \frac{dp_{lx}}{dx} . \tag{15}$$

Here, the first term is associated with the electroosmotic flow, where n_w is the electroosmotic transfer number for water, j_p is the flow of protons (per unit of the external surface of the membrane and the membrane-electrode assembly) that have appeared in electrode reactions. The second term is associated with the Darcy convective flow, where c_w is the number of water molecules in unit volume, μ is the water viscosity coefficient, $K(v_x)$ is the membrane permeability coefficient found based on the Hagen–Poiseuille–Kozeni equation

$$K(v_x) = \xi \frac{(v - v_b)\, v(r)}{8} \Theta(v - v_b) , \tag{16}$$

where x is the tortuosity factor, v_b is the moisture content threshold for which the continuity of liquid-filled pores is violated, $v(r)$ is the function of moisture content distribution over radii, Θ is the Heaviside step function.

Taking into account the water stoichiometry in the chemical reaction, the resulting water flow through the membrane is expressed by the relationship

$$j_m = j_a = j_c - \frac{1}{2} j_n . \quad (17)$$

The quantities j_a and j_c (per unit of the external surface of membrane and membrane-electrode assembly) are determined by the external flows of water vapour in the anodic and cathodic gas chambers of FC. The equation for the voltammetric characteristic is derived based on the Ohm law

$$j_p = -\frac{k(v_x)}{e} \frac{d\eta}{dx}, \quad (18)$$

where $k(v_x)$ is conductivity.

Numerical solution of the above system of equations affords the voltammertic characteristics for a FC with proton-conducting membrane in the approximation of low anodic and cathodic polarization values [152] by taking into account the external exchange of moisture. Since this system involves moisture content distribution functions over radii and the isotherm of capillary pressures, then they obviously have a substantial effect on voltammetric characteristics. The analysis of this system has shown that for a certain (high) current density, the moisture content in the membrane on its anodic side approaches zero, which brings about the sharp increases in ohmic losses. This current density is limiting ($j_{p\,lim}$) for the water removal from the cathode where it has been generated. To increase $j_{p\,lim}$ and optimize the voltammetric characteristics, one must observe the water balance conditions according to which water is fed to the anode and its excess is removed from the cathode. Thus, the water management problem can be solved by applying this mathematical model.

The experimental electrochemical characteristics of proton-exchange membrane FC were found to be adequately consistent with characteristics calculated by the aforementioned method.[152] Furthermore, good agreement was observed [166] between the experimental data and those calculated in terms of the described model.[152]

Unlike the above approach to solving the water management problem by applyig the Darcy equation to the water flow in a membrane under the capillary pressure gradient,[152] in several publications the analogous problem was solved by considering the equation of water diffusion in a membrane under the effect of water concentration gradient (*e.g.*, see Refs 161, 164, 165). The latter approach is insufficiently substantiated for two reasons. First, the consideration of water diffusion with respect to the stationary polymer matrix in a membrane is questionable. Second, in this case the concept of the water diffusion coefficient becomes meaningless, in contrast to the permeability coefficient which is used in the former approach based on the Hagen–Poiseuille–Kozeni equation and the curve of moisture content distribution over membrane pore radii.

3. Membrane-electrode assembly

In fuel cells of the matrix type, the electrolyte or water are contained only in pores of components of the membrane-electrode assembly. The electrochemical characteristics of the membrane-electrode assembly and of the whole FC are known to depend on the moisture content (water volume) or the electrolyte content (volume). The electrochemical flooding curves, *i.e.*, the dependences of the FC voltage (U) on the water content, were measured.[157] This brings about the problem of simulating the electrochemical curves of flooding taking into account the porous structure of components of the membrane-electrode assembly. This problem and also the problem of water content optimization can be solved by using the experimental method of standard contact porosimetry and the theory of capillary processes that lies in the basis of this method.[158–160]

Polarization (η_i) of each component in the membrane-electrode assembly, namely, its gas-diffusion layer, catalyst, membrane, *etc.*, depends on the moisture content (v_i), *i.e.*, on the degree of flooding of pores with water or electrolyte. The dependences

$$\eta_i = \psi_i (v_i) \quad (19)$$

(shown here for the constant current density per unit external surface of the assembly) can be calculated based on macrokinetics of processes in porous electrodes and membranes [56, 109, 153–156] and were measured experimentally.[53] Figure 30 presents the electrochemical curves of flooding for catalytic and gas-diffusion layers and also for the membrane of a hydrogen–oxygen FC plotted in the the $\eta-\omega$ coordinates. Curve *2* for the catalytic layer has a minimum. For small ω, the polarization is high due to ohmic losses; for large ω, polarization is high due to concentration polarization determined by the diffusion of active gases (H_2 or O_2). The minimum region corresponds to optimal ω. Curves *1* and *3* are monotonic. For the gas-diffusion layer, the high polarization values are possible only in the region of high ω, which is associated with concentration polarization due to diffusion of active gases, whereas for the membrane the high polarization region is observed only at low ω values due to the high ohmic losses.

For each component of the membrane-electrode assembly, it is possible to measure the isotherms of capillary pressure by standard contact porosimetry

$$v_i = f_i (p_{ci}). \quad (20)$$

Figure 28 shows such experimental isotherms of capillary pressure for a Nafion 117 membrane.

According to thermodynamics of capillary processes, in a membrane-electrode assembly in the capillary equilibrium state (as well as in the clamping device used in the standard contact porosimetry, see Section II.3.a), the p_{ci} values are equal for all components i

$$p_{c1} = p_{c2} = \ldots p_{ci} \equiv p_c . \quad (21)$$

Taking into account Eqns (19), (20), the value n in the whole assembly is

$$v = \sum v_i = \sum f_i(p_{ci}) \equiv F(p_c). \quad (22)$$

This makes it possible to obtain the inverse function of p_c on n:

$$p_c = F^{-1}(v). \quad (23)$$

It follows from Eqns (19)–(23) that

$$v_i = f_i F^{-1}(v) . \quad (24)$$

Based on relationships (19) and (24), we obtain

$$\eta_i = \psi_i F^{-1}(v) . \quad (25)$$

Insofar as the voltage in the membrane-electrode assembly is

$$U = E_{\text{emf}} - \sum \eta_i \tag{26}$$

(E_{emf} is the thermodynamic electromotive force), then

$$U = E_{\text{emf}} - \sum \psi_i F^{-1}(v)\,. \tag{27}$$

This function describes the electrochemical curves of flooding for assembly components at a constant current. Based on this theoretical approach, the graphical method of calculating and optimizing the flooding curves has been developed,[158–160] which involves plotting a set of structural-and-electrochemical curves including porograms and flooding curves for all components of the assembly. It was also analyzed how the mutual arrangement of porosimetric curves of membrane-electrode assembly components affects the electrochemical curves of flooding of the FC as a whole, which allowed the optimization conditions for the mutual arrangement of assembly components to be developed.

The following examples of capillary incompatibility of various assembly components can be shown. If due to deviations in porosimetric curves for anodic and cathodic catalytic layers, their minima occur in different n regions on the scale of total electrolyte volume, then at some v one layer is flooded and the other remains too dry. This means the capillary incompatibility of these catalytic layers even if they exhibit high catalytic activity. On the other hand, if the membrane has too coarse pores as compared with pores in the catalytic layers, then it will be too dry in the vicinity of electrode flooding curve minima and, hence, its polarization will be too high. Moreover, for a capillary membrane, the danger of explosion can emerge: the too large volume of coarse pores can turn out to be free of electrolyte and give room for mixing hydrogen and oxygen.[158–160]

These examples illustrate the necessity of mutual optimization of the porous structure and hydrophilic-hydrophobic properties of all components of the membrane-electrode assembly. Optimization of this type can, in principle, be applied to various types of FC including the microfluidized FC that can operate on biofuel and are being developed recently.[167] In the latter FC, the hydrodynamic flows of reagents and electrolyte are organized; however, there are no enough data on the porous structure of their components.

VI. Conclusion

This review discusses the results of studying the porous structure and hydrophilic-hydrophobic properties of the following components of the membrane-electrode assembly of fuel cells: ion-exchange and capillary membranes, polymer hydrophobizers, catalytic and gas-diffusion layers. These studies were carried out mainly by the method of standard contact porosimetry which, in contrast to other methods, provides a lot of information on the porous structure, including the data on pore corrugation and the specific surface area and also on the swelling of multicomponent and powder materials in the widest range of pore sizes (from ~ 1 to 3×10^5 nm) and their hydrophilic-hydrophobic properties. Moreover, this method makes it possible to measure adsorption (desorption) isotherms, capillary pressure isotherms and binding energy isotherms (energy isotherms). By means of standard contact porosimetry, it is possible to carry out measurements under conditions that resemble most closely the fuel cell operation conditions, namely, at the same temperatures, compression pressures and in contact with electrolyte or water. The latter factor is very important, because it takes into account the real swelling of components of the membrane-electrode assembly.

This review describes the recently discovered phenomenon of inversion of ionomer ion-exchange groups in catalytic layers, which affects the hydrophilic-hydrophobic properties and the efficiency of fuel cell operation. A theoretical study was carried out of how the porous structure and hydrophilic-hydrophobic properties of membrane-electrode assembly components affect the electrochemical characteristics of fuel cells. The results of studies surveyed in this review have already found application in the development and optimization of electrochemical generators. This is why we hope that publication of this review will be beneficial for wider practical application of these results.

References

1. *Handbook of Fuel Cells. Fundamentals Technology and Applications* V. 1–4 (Eds W Vielstich, A Lamm, H A Gasteiger) (Chichester: Wiley, 2003)
2. V S Bagotsky *Fuel Cells: Problems and Solutions* (Hoboken, NJ: Wiley, 2009)
3. E F Medici, J S Allen *J. Electrochem. Soc. B* **157** 1505 (2010)
4. J Rouquerol, G Baron, R Denoyel, H Giesche, J Groen, P Klobes, P Levitz, A V Neimark, S Rigby, R Skudas, K Sing, M Thommes, K Unger *Pure Appl. Chem.* **84** 107 (2012)
5. C Drake *Ind. Eng. Chem.* **1** 780 (1949)
6. F Gomez, R Denoyel, J Rouquerol *Langmuir* **16** 3474 (2000)
7. B Lefevre, A Saugey, J-L Barrat, L Bocquet, E Charlaix, P F Gobin, G Vigier *J. Chem. Phys.* **120** 4927 (2004)
8. A Jena, K Gupta *Fluid Part. Separat. J.* **4** 227 (2002)
9. A Y Fadeev, V Eroshenko *J. Colloid Interface Sci.* **187** 275 (1997)
10. V Eroshenko, R-C Regis, M Soulard, J Patarin *J. Am. Chem. Soc.* **123** 8129 (2001)
11. M M Dubinin, G M Plavnik *Carbon* **6** 183 (1968)
12. S Miklos, A Pohl *Bergakademie* **22** 97 (1970)
13. M J Swata, I Jansta *Czech. Chem. Commun.* **30** 2455 (1965)
14. B Miller, I Tyomkin *J. Colloid Interface Sci.* **162** 163 (1994)
15. S J Gregg, K S W Sing *Adsorption, Surface Area and Porosity* (New York: Academic Press, 1967)
16. D S Watkins *Fuel Cell Systems* (New York: Plenum, 1993)
17. R Schlögl, H Schuring *Z. Elektrochem.* **10** 863 (1961)
18. J Tersoff, D R Hamann *Phys. Rev.* **31** 805 (1985)
19. J Bardeen *Phys. Rev. Lett.* **6** 57 (1961)
20. P Dietz, P K Hansma, O Inacker *J. Membr. Sci.* **65** 101 (1992)
21. E K Lavrentyeva, S Y Vassiliev, A A Tsirlin, S N Plyakov, M Leoni, K S Napolskii, O A Petrii, G A Tsirlina *Electrochim. Acta* **61** 94 (2012)
22. M R Tarasevich, A V Kuzov, A L Klyuev, V N Titova *Elektrokhim. Energet.* **7** 156 (2007)
23. E W Washburn *Phys. Rev.* **18** 273 (1921)
24. V Gurau, M J Bluemle, E S De Castro, Y M Tsou, J A Mann, T A Zawodzinski *J. Power Sources* **160** 1156 (2006)
25. L Labajos-Broncano, M L Gonzalez-Marttn, J M Bruque, C M Gonzalez-Garcia *J. Colloid Interface Sci.* **234** 79 (2001)
26. A Hamraoui, T Nylander *J. Colloid Interface Sci.* **250** 415 (2002)

27. B R Friess, M Shahraeeni, M Hoorfar, in *Proceedings of 2008 AIChE Conference, Philadelphia, 2008* p. 337
28. K Grundke, A Augsburg, J Adhes *Sci. Technol.* **14** 765 (1999)
29. J Troger, K Lunkwitz, K Grundke, B Wolfgang *Physiochem. Eng. Asp.* **134** 299 (1997)
30. K Grundke, T Bogumil, T Gietzelt, H-J Jacobasch, D Y Kwok, A W Neumann *Prog. Colloid Polym. Sci.* **101** 58 (1996)
31. B R Friess, M Hoorfar *J. Power Sources* **195** 4736 (2010)
32. Yu M Vol'fkovich, V E Sosenkin *Dokl. Akad. Nauk SSSR* **234** 125 (1977) [a]
33. Yu M Vol'fkovich, E I Shkol'nikov *Zh. Fiz. Khim.* **52** 210 (1978) [b]
34. Yu M Vol'fkovich, E I Shkol'nikov *Elektrokhimiya* **15** 8 (1979) [c]
35. Y M Volfkovich, V S Bagotsky *J. Power Sources* **48** 327 (1994)
36. Y M Volfkovich, V S Bagotsky *J. Power Sources* **48** 339 (1994)
37. Y M Volfkovich, V S Bagotsky, V E Sosenkin, I A Blinov *Colloids Surf., A* **187**–**188** 349 (2001)
38. Yu M Vol'fkovich, V S Bagotskii, V E Sosenkin, E I Shkol'nikov *Elektrokhimiya* **16** 1620 (1980) [c]
39. US P. 6298711 (2001)
40. US P. 7059175 (2006)
41. O A Baturina, Y M Volfkovich, A V Sakars, K J Wynne, G E Wnek *The 207th Meeting of the Electrochemical Society. Meeting Abstracts, Quebec, Canada, 2005*
42. Yu M Vol'fkovich, V E Sosenkin, N F Nikol'skaya *Elektrokhimiya* **46** 352 (2010) [c]
43. Yu M Vol'fkovich, V E Sosenkin, N F Nikol'skaya *Elektrokhimiya* **46** 462 (2010) [c]
44. Y M Volfkovich, V E Sosenkin, V S Bagotsky *J. Power Sources* **195** 5429 (2010)
45. S Gottesfeld, T A Zawodzinski, in *Advances in Electrochemical Science and Engineering* Vol. 5 (Eds R C Alkire, H Gerischer, D M Kolb, C W Tobias) (Weinheim: Wiley-VCH, 1997) p. 195
46. Yu M Vol'fkovich, V E Sosenkin, A Yu Rychagov, N F Nikol'skaya, in *Sovremennye Problemy Fizicheskoi Khimii Nanomaterialov* (Current Problems of Physical Chemistry of Nanomaterials) (Ed. A Yu Tsivadze) (Moscow: A N Frumkin Institute of Physical Chemistry and Electrochemistry, Russian Academy of Sciences, 2008) p. 532
47. Yu M Vol'fkovich, N A Kononenko, M A Chernyaeva, M M Kardash, A I Shkabara, A V Pavlov *Kriticheskie Tekhnologii. Membrany* **39** 8 (2008)
48. K S Napolskii, P J Barczuk, S Y Vassiliev, A G Veresov, G A Tsirlina, P J Kulesza *Electrochim. Acta* **52** 7910 (2007)
49. T Kyotani, W H Xu, Y Yokoyama *J. Membr. Sci.* **196** 231 (2002)
50. T D Gladysheva, E I Shkol'nikov, Yu M Vol'fkovich, B I Podlovchenko *Elektrokhimiya* **18** 435 (1982) [c]
51. B B Damaskin, O A Petrii, G A Tsirlina, in *Elektrokhimiya* (Electrochemistry) (Moscow: Khimiya, KolosS, 2008) p. 593
52. B I Podlovchenko, T D Gladysheva, O V Vyaznikovtseva, Yu M Vol'fkovich *Elektrokhimiya* **19** 424 (1983) [c]
53. Yu M Vol'fkovich, E I Shkol'nikov, V S Dubasova, V A Ponomarev *Elektrokhimiya* **19** 765 (1983) [c]
54. M A Khrizolitova, Yu M Vol'fkovich, G V Mikhaleva, L S Tabakman *Elektrokhimiya* **24** 766 (1988) [c]
55. Yu M Vol'fkovich, E I Shkol'nikov *Elektrokhimiya* **19** 586 (1983) [c]
56. Yu M Vol'fkovich, E I Shkol'nikov *Elektrokhimiya* **19** 1199 (1983) [c]
57. T Soboleva, X Zhao, K Malek, Z Xie, T Navessin, S Holdcroft *ACS Appl. Mater. Interfaces* **2** 375 (2010)
58. J H Kim, J S Yu *Chem. Phys.* **12** 15301 (2010)
59. V Rao, P A Simonov, E R Savinova, G V Plaksin, S V Cherepanova, G N Kryukova, U Stimming *J. Power Sources* **145** 178 (2005)
60. Y Takasu, T Kawaguchi, W Sugimoto, Y Marukami *Electrochim. Acta* **48** 3861 (2003)
61. G S Chai, I-S Shin, J-S Yu *Adv. Mater.* **16** 2057 (2004)
62. G S Chai, S B Yoon, J-S Yu, J-H Choi, Y-E Sung *J. Phys. Chem. B* **108** 7074 (2004)
63. F Su, X-S Zhao, Y Wang, J Zeng, Z Zhou, J Y Lee *J. Phys. Chem. B* **109** 20200 (2005)
64. H Shioyama, A Ueda, N Kuriyama *J. New Mater. Electrochem. Syst.* **10** 201 (2007)
65. G Wu, Y-Sh Chen, B-Q Xu *Electrochem. Commun.* **7** 1237 (2005)
66. E Frackowiak, G Lot, T Cacciaguerra, F Beguin *Electrochem. Commun.* **8** 129 (2006)
67. D-J Guo, H-L Li *J. Power Sources* **160** 44 (2006)
68. C-H Wang, H-C Shih, Y-T Tsai, H-Y Du, L-C Chen, K-H Chen *Electrochim. Acta* **52** 1612 (2006).
69. J Prabhuram, T S Zhao, Z X Liang, R Chen *Electrochim. Acta* **52** 2649 (2007)
70. C-C Chen, C-F Chen, C-M Chen, F-T Chuang *Electrochem. Commun.* **9** 159 (2007)
71. M-C Tsai, T-K Yeh, C-H Tsai *Electrochem. Commun.* **8** 1445 (2006)
72. H J Wang, H Yu, F Peng, P Lv *Electrochem. Commun.* **8** 499 (2006)
73. E K Tuseeva, N A Maiorova, V E Sosenkin, N F Nikol'skaya, Yu M Vol'fkovich, A V Krestinin, G I Zvereva, V A Grinberg, O A Khazova *Elektrokhimiya* **44** 955 (2008) [c]
74. N A Maiorova, E K Tuseeva, V E Sosenkin, A Yu Rychagov, Yu M Vol'fkovich, A V Krestinin, G I Zvereva, O M Zhigalina, O A Khazova *Elektrokhimiya* **45** 1168 (2009) [c]
75. M Q Tran, J T Cabral, M S P Shaffer, A Bismarck *Nano Lett.* **8** 2744 (2008)
76. A V Bazilevsky, K Sun, A L Yarin, C M Megaridis *J. Mater. Chem.* **18** 696 (2008)
77. J Kong, Y Xu, K-L Yung, Y Xie, L He *J. Phys. Chem. C* **113** 624 (2009)
78. Z Insepov, D Wolf, A Hassanein *Nano Lett.* **6** 1893 (2006)
79. P Kim, H-Y Kim, J K Kim, G Reiter, K Y Suh *Lab-on-a-Chip* **9**3255 (2009)
80. D I Dimitrov, A Milchev, K Binder *Langmuir* **24** 1232 (2008)
81. S Bekou, D Mitta *Curr. Opin. Colloid Interface Sci.* **16** 259 (2011)
82. E Dujardin, T W Ebbesen, H Hiura, K Tanigaki *Science* **265** 1850 (1994)
83. D Ugarte, T Stöckli, J M Bonard, A Chtelain, W A Heer *Appl. Phys. A* **67** 101(1998)
84. D Mattia, Y Gogotsi *Microfluid Nanofluid* **5** 289 (2008)
85. Y Li, J Xu, D Li *Microfluid Nanofluid* **9** 1011 (2010)
86. V M Starov, M G Velarde, C J Radke *Surfactant Science Series* (Boca Raton, FL: CRC Press, 2007)
87. J S Aluru *Nano Lett.* **8** 452 (2008)
88. M P Brenner, D Lohse *Phys. Rev. Lett.* **101** 214505 (2008)
89. B V Derjagin, N V Churaev, V M Muller *Surface Forces. Consultants Bureau* (New York: Plenum, 1987)
90. W F Lin, M S Zei, M Eiswirth, G Ertl, T Iwasita, W Vielstich *J. Phys. Chem.* **103** 6968 (1999)
91. F Delime, J-M Leger, C Lamy *J. Appl. Electrochem.* **28** 27 (1998)
92. C L Green, A Kucernak *J. Phys. Chem. B* **106** 1036 (2002)
93. C L Green, A Kucernak *J. Phys. Chem. B* **106** 11446 (2002)
94. G Wu, L Li, J-H Li, B-Q Xu *J. Power Sources* **155** 118 (2006)
95. P Santosh, A Gopalan, K-P Lee *J. Catal.* **234** 177 (2006)
96. C Jiang, X Lin *J. Power Sources* **164** 49 (2007)
97. Z A Hu, L J Ren, X J Feng, Y P Wang, Y Y Yang, J Shi, L P Mo, Z Q Lei *Electrochem. Commun.* **9** 97 (2007)
98. B I Podlovchenko, V N Andreev *Russ. Chem. Rev.* **71** 837 (2002) [*Usp. Khim.* **71** 950 (2002)]

99. Yu M Maksimov, E A Kolyadko, A V Shishlova, B I Podlovchenko *Elektrokhimiya* **37** 907 (2001) [c]
100. B I Podlovchenko, A V Smolin, Yu M Maksimov *Elektrokhimiya* **31** 1174 (1995) [c]
101. P O Esteban, J M Leger, C Lamy, E Genis *J. Appl. Electrochem.* **19** 462 (1989)
102. K Kost, D Bartak, B Kazee, T Kuwana *Anal. Chem.* **60** 2379 (1988)
103. J Li, D Petelenz, J Yanata *Electroanalysis* **5** 791 (1993)
104. A A Mikhailova, E B Molodkina, O A Khazova, V S Bagotsky *J. Electroanal. Chem.* **509** 1 (2001)
105. Y M Volfkovich, V S Bagotsky, T K Zolotova, E Y Pisarevskaya *Electrochim. Acta* **48** 1905 (1996)
106. Y M Volfkovich, M D Levi, T K Zolotova, E Y Pisarevskaya *Polym. Commun.* **34** 2443 (1993)
107. Y M Volfkovich, T K Zolotova, M D Levi, Y A Letuchy *Adv. Mater.* **5** 274 (1993)
108. Y M Volfkovich, A G Sergeev, T K Zolotova, S D Afanasiev, O N Efimov, E P Krinichnaya *Electrochim. Acta* **44** 1543 (1999)
109. Yu A Chizmadzhev, V S Markin, M R Tarasevich, Yu G Chirkov *Makrokinetika Protsessov v Poristykh Sredakh* (Macrokinetics of Processes in Porous Media) (Moscow: Nauka, 1971)
110. A S Lipilin *Elektrokhim. Energet.* **7** 61 (2007)
111. B Kenney, K Karan *Solid State Ionics* **178** 297 (2007)
112. H Zhu, R J Kee *J. Electrochem. Soc.* **155** B715 (2008)
113. J R Wilson, A T Duong, M Gameiro, H Y Chen, K Thornton, D R Mumm, S A Barnett *Electrochem. Commun.* **11** 1052 (2009)
114. J R Wilson, W Kobsiriphat, R Mendoza, H Y Chen, J M Hiller, D J Miller, K Thornton, P W Voorhees, S B Adler, S A Barnett *Nature (London)* **5** 541 (2006)
115. Y Suzue, N Shikazono, N Kasagi *J. Power Sources* **184** 52 (2008)
116. J H Nam, D H Jeon *Electrochim. Acta* **51** 3446 (2006)
117. P Costamagna, P Costa, V Antonucci *Electrochim. Acta* **43** 375 (1998)
118. C Nicolella, A Bertei, M Viviani, A Barbucci *J. Appl. Electrochem.* **39** 503 (2009)
119. B Kenney, M Valdmanis, C Baker, J G Pharoah, K Karan *J. Power Sources* **189** 1051 (2009)
120. I V Belova, G E Murch *J. Phys. Chem. Solids* **66** 722 (2005)
121. R Al-Raoush, M Alsaleh *Powder Technol.* **176** 47 (2007)
122. D Chen, Z Lin, H Zhu, R J Kee *J. Power Sources* **191** 240 (2009)
123. M Suzuki, T Oshima *Powder Technol.* **35** 159 (1983)
124. D Bouvard, F F Lange *Acta Metall. Mater.* **39** 3083 (1991)
125. A Bertei, C Nicolella *J. Power Sources* **196** 9429 (2011)
126. J Divisek, R Wilkenhtsner, Y M Volfkovich *J. Appl. Electrochem.* **29** 153 (1999)
127. S Cordiner, S P Lanzani, V Mulone *Int. J. Hydrogen Energy* **36** 10366 (2011)
128. L Cindrella, A M Kannan, J F Lin, K Saminathan, Y Ho, C W Lin, J Wertz *J. Power Sources* **194** 146 (2009)
129. E Antolini, R R Passos, E A Ticianelli *J. Appl. Electrochem.* **32** 383 (2002)
130. S E Iyuke, A B Mohamad, A A H Kadhum, W R W Daud, C Rachid *J. Power Sources* **114** 195 (2003)
131. H S Park, Y H Cho, C R Jung, J H Jang, Y E Sung *Electrochim. Acta* **53** 763 (2007)
132. S Shimpalee, U Beuscher, J W van Zee *J. Power Sources* **163** 480 (2006)
133. J H Jang, W M Yan, C C Shih *J. Power Sources* **161** 323 (2006)
134. M Coppo, N P Siegel, M R von Spakovsky *J. Power Sources* **159** 560 (2006)
135. J X Wu, Q Y Liu *J. Fuel Cell Sci. Technol.* **2** 20 (2005)
136. G Inoue, T Yoshimoto, Y Matsukuma, M Minemoto *J. Power Sources* **175** 145(2008)
137. W C Weng, W M Yan, H Y Li, X D Wang *J. Electrochem. Soc.* **155** B877 (2008)
138. K P Adzakpa, K Agbossou, Y Dube, M Dostie, M Fournier, A Poulin *IEEE Trans. Energy Convers.* **23** 581 (2008)
139. M Secanell, K Karan, A Suleman, N Djilali *J. Electrochem. Soc.* **155** B125 (2008)
140. S M Chang, H S Chu *J. Power Sources* **172** 790 (2007)
141. A A Shah, G S Kim, W Gervais, A Young, K Promislow, J Li, S Ye *J. Power Sources* **160** 1251 (2006)
142. C H Liu, T H Ko, J W Shen, S I Chang, S I Chang, Y K Liao *J. Power Sources* **191** 489 (2009)
143. M V Williams, E Begg, L Bonville, H R Kunz, J M Fenton *J. Electrochem. Soc.* **151** A1173 (2004)
144. Yu M Vol'fkovich, V E Sosenkin, N F Nikol'skaya, T L Kulova *Elektrokhimiya* **44** 300 (2008) [c]
145. J T Gostik, M W Fowler, M A Ioannidis, M D Pritzker, Y M Volfkovich, A V Sakars *J. Power Sources* **156** 375 (2006)
146. J Farmer, B Duong, S Seraphin, S Shimpalee, M J Martinez-Rodriguez, J W van Zee *J. Power Sources* **197** 1 (2012).
147. V S Bagotsky, Y M Volfkovich *J. Appl. Electrochem.* **2** 315 (1972)
148. Yu M Vol'fkovich, V K Luzhin, A N Vanyulin, E I Shkol'nikov, I A Blinov *Elektrokhimiya* **20** 656 (1984) [c]
149. Yu M Vol'fkovich, N A Dreiman, O N Belyaeva, I A Blinov *Elektrokhimiya* **24** 352 (1988) [c]
150. Yu J Divisek, M Eikerling, V M Mazin, H Schmitz, U Stimming, Y M Volfkovich *J. Electrochem. Soc.* **145** 2677 (1998)
151. N P Berezina, Yu M Vol'fkovich, N A Kononenko, I A Blinov *Elektrokhimiya* **23** 912 (1987) [c]
152. M Eikerling, Y I Kharkats, A A Kornyshev, Y M Volfkovich *J. Electrochem. Soc.* **145** 2684 (1998)
153. I G Gurevich, Yu M Vol'fkovich, V S Bagotskii *Zhidkostnye Poristye Elektrody* (Liquid Porous Electrodes) (Minsk: Nauka i Tekhnika, 1974)
154. Yu M Vol'fkovich, E I Shkol'nikov *Elektrokhimiya* **19** 656 (1983) [c]
155. Yu M Vol'fkovich, E I Shkol'nikov *Elektrokhimiya* **19** 757 (1983) [c]
156. T F Fuller, J Newman *J. Electrochem. Soc.* **140** 1218 (1993)
157. V E Sosenkin, Yu M Vol'fkovich, V S Bagotskii *Elektrokhimiya* **9** 514 (1973) [c]
158. Yu M Vol'fkovich *Elektrokhimiya* **14** 546 (1978) [c]
159. Yu M Vol'fkovich *Elektrokhimiya* **14** 831 (1978) [c]
160. Yu M Vol'fkovich *Elektrokhimiya* **14** 1477 (1978 [c]
161. B Dokkar, N E Settou, O Imine, N Saifi, B Negrou, Z Nemouchi *Int. J. Hydrogen Energy* **36** 4220 (2011)
162. N Akhtara, S P Decenta, K Kendallb *J. Power Sources* **195** 7796 (2010)
163. C H Cheng, K Fei, C W Hong *Comp. Chem. Eng.* **31** 247 (2007)
164. J Ramousse, J Deseure, O Lottin, S Didierjean, D Maillet *J. Power Sources* **145** 416 (2005)
165. R Sousa, E R Gonzalez *J. Power Sources* **147** 32 (2005)
166. R F Mann, J C Amphlett, M A I Hooper, H M Jensen, B A Peppley, P R Roberge *J. Power Sources* **86** 173 (2000)
167. E Kjeang, N Djilali, D Sinton *J. Power Sources* **186** 353 (2009)

[a] — *Dokl. Phys. Chem. (Engl. Transl.)*
[b] — *Russ. J. Phys. Chem., Ser. A (Engl. Transl.)*
[c] — *Russ. J. Electrochem. (Engl. Transl.)*